Supplementary Information for

Reaching the Efficiency Limit of Arbitrary Polarization Transformation with Non-orthogonal Metasurfaces

Yueyi Yuan[1], Kuang Zhang[1,*], Qun Wu[1], Shah Nawaz Burokur[2,*] and Patrice Genevet[3,*]

[1] Department of Microwave Engineering, Harbin Institute of Technology, 150001 Harbin, China.

[2] LEME, UPL, Univ Paris Nanterre, 92410 Ville d'Avray, France.

[3] Physics department, Colorado School of Mines, 1523 Illinois St, Golden, CO 80401, USA

E-mail: zhangkuang@hit.edu.cn, sburokur@parisnanterre.fr, patrice.genevet@mines.edu

Note 1. Derivations and analyses of Jones matrix with general form

1.1 Jones matrix in general form with Jordan decomposition

In this work, we focus on the polarization information of electromagnetic (EM) wave, which is described by the motion trajectory of electric field. When we ignore the time-harmonic property and the overall responses, the plane wave can be simplified with only normalized amplitude and relative phase delay, as follows:

$$\left|\vec{\boldsymbol{E}}\right\rangle = \begin{bmatrix} E_x e^{i\delta_x} \\ E_y e^{i\delta_y} \end{bmatrix} = \begin{bmatrix} \cos\alpha \\ \sin\alpha \cdot e^{i\beta} \end{bmatrix} \tag{S1}$$

where $\left|\vec{\boldsymbol{E}}\right\rangle$ is in the Jones vector notation, α = arctan (E_y / E_x), and $\beta = \delta_y - \delta_x$ represents two Jones variables to illustrate the trajectory shape of the electric field and determine the polarization of EM wave. The geometric representation of polarizations, including all fundamental linear, circular, elliptical states, can be characterized in a unit sphere by Jones vectors, termed as "Poincaré sphere". The Stokes parameters [S_1, S_2, S_3] are adopted to provide a straightforward connection between geometric elliptical angles (azimuth angle 2φ and declination angle 2χ on Poincaré sphere) and Jones variables:

$$\begin{cases} \tan 2\varphi = \tan 2\alpha \cos\beta \\ \sin 2\chi = \sin 2\alpha \sin\beta \end{cases} \tag{S2}$$

When a monochromatic plane EM wave passes through a polarizing medium, the polarization state of output wave depends on the input polarization state and the polarization properties of the medium or devices. The polarizing properties can then be described by a complex 2 × 2 Jones matrix with linear base as $\boldsymbol{J} = \begin{bmatrix} J_{xx} & J_{xy} \\ J_{yx} & J_{yy} \end{bmatrix}$, where subscripts show the linearly polarized output and input states, and four different complex coefficients represent the preserving or conversion abilities with orthogonal linearly polarization states. As known, the eigen polarization states $\left|\zeta_{1,2}\right\rangle = \begin{bmatrix} \zeta_{1x,2x} \\ \zeta_{1y,2y} \end{bmatrix}$ of Jones matrix embody the intrinsic steady states that would not be disturbed when passing through the polarizing medium, while the corresponding eigen-values $\kappa_{1,2}$ just scale the eigen-states with amplitude and phase profiles. Here, we analyze general eigen-formalism, including eigen-values and eigen-states, according to $\boldsymbol{J} \cdot \left|\zeta_{1,2}\right\rangle = \boldsymbol{\kappa}_{1,2} \left|\zeta_{1,2}\right\rangle$, which can be solved by:

$$\kappa_{1,2} = \frac{\left(J_{xx} + J_{yy}\right) \pm \sqrt{\left(J_{xx} - J_{yy}\right)^2 + 4J_{xy}J_{yx}}}{2} \tag{S3}$$

where "±" denotes two distinct eigen-values. It is noted that the Jones matrix discussed in our work just relate to the normal form that $\kappa_1 \neq \kappa_2$, and except for the defective Jones matrix with $\kappa_1 = \kappa_2$. Thus, there are two distinct eigen-states with normalization that can be derived as:

$$\begin{cases} |\zeta_1\rangle = \begin{bmatrix} 1 \\ \dfrac{-\left(J_{xx}-J_{yy}\right)+\sqrt{\left(J_{xx}-J_{yy}\right)^2+4J_{xy}J_{yx}}}{2J_{xy}} \end{bmatrix} = \begin{bmatrix} \cos\alpha_1 \\ \sin\alpha_1 \cdot e^{i\beta_1} \end{bmatrix} \\ |\zeta_2\rangle = \begin{bmatrix} \dfrac{\left(J_{xx}-J_{yy}\right)+\sqrt{\left(J_{xx}-J_{yy}\right)^2+4J_{xy}J_{yx}}}{2J_{yx}} \\ 1 \end{bmatrix} = \begin{bmatrix} \cos\alpha_2 \\ \sin\alpha_2 \cdot e^{i\beta_2} \end{bmatrix} \end{cases} \tag{S4}$$

Based on Eq. (S4), we apply an invertible 2 × 2 matrix that is composed of two eigen-states as columns $\boldsymbol{Q} = \begin{bmatrix} \zeta_{1x} & \zeta_{2x} \\ \zeta_{1y} & \zeta_{2y} \end{bmatrix}$ and a diagonalized matrix $\boldsymbol{P} = \begin{bmatrix} \kappa_1 & 0 \\ 0 & \kappa_2 \end{bmatrix}$ with two eigen-values located in the diagonal position to implement the Jordan decomposition of Jones matrix:

$$\begin{aligned} \boldsymbol{J} = \boldsymbol{QPQ}^{-1} &= \begin{bmatrix} \zeta_{1x} & \zeta_{2x} \\ \zeta_{1y} & \zeta_{2y} \end{bmatrix} \begin{bmatrix} \kappa_1 & 0 \\ 0 & \kappa_2 \end{bmatrix} \begin{bmatrix} \zeta_{1x} & \zeta_{2x} \\ \zeta_{1y} & \zeta_{2y} \end{bmatrix}^{-1} \\ &= \frac{\kappa_1}{\Delta} \begin{bmatrix} \zeta_{1x}\zeta_{2y} & -\zeta_{1x}\zeta_{2x} \\ \zeta_{1y}\zeta_{2y} & -\zeta_{1y}\zeta_{2x} \end{bmatrix} + \frac{\kappa_2}{\Delta} \begin{bmatrix} -\zeta_{1y}\zeta_{2x} & \zeta_{1x}\zeta_{2x} \\ -\zeta_{1y}\zeta_{2y} & \zeta_{1x}\zeta_{2y} \end{bmatrix} \end{aligned} \tag{S5}$$

where $\Delta = \zeta_{1x}\zeta_{2y} - \zeta_{2x}\zeta_{1y}$. On the other hand, the Jones matrix can also be expressed with Jones variables α and β:

$$\boldsymbol{J} = \frac{\kappa_1}{\Delta'} \begin{bmatrix} \cos\alpha_1 \sin\alpha_2 e^{i\beta_2} & -\cos\alpha_1 \cos\alpha_2 \\ \sin\alpha_1 \sin\alpha_2 e^{i(\beta_1+\beta_2)} & -\sin\alpha_1 \cos\alpha_2 e^{i\beta_1} \end{bmatrix} + \frac{\kappa_2}{\Delta'} \begin{bmatrix} -\sin\alpha_1 \cos\alpha_2 e^{i\beta_1} & \cos\alpha_1 \cos\alpha_2 \\ -\sin\alpha_1 \sin\alpha_2 e^{i(\beta_1+\beta_2)} & \cos\alpha_1 \sin\alpha_2 e^{i\beta_2} \end{bmatrix} \tag{S6}$$

where $\Delta' = \cos\alpha_1 \sin\alpha_2 e^{i\beta_2} - \sin\alpha_1 \cos\alpha_2 e^{i\beta_1}$. From Eqs. (S5) and (S6), we can observe that the polarization control ability of elements or systems physically depends on eigen-states and eigen-values.

1.2 Inhomogeneity of Jones matrix

According to the orthogonality of two eigen-states, the Jones matrix can be divided into homogeneous and inhomogeneous. When the two eigen-states are orthogonally linear, circular, or elliptical, the corresponding Jones matrix is defined as homogeneous. Such scheme is adapted to the most situations of current meta-polarizers and meta-devices, which are composed of single-layered meta-atoms with in-plane rotational or non-rotational symmetricity (constructed by sole element or polyatomic elements), analogue to the individual waveplate or polaroid, as schematically shown in Fig. 1A of main text. By contrast, the non-orthogonal eigen-state pair defines inhomogeneous Jones matrix that are profitable for more general situations in optical systems with cascading multiple waveplates or lenses, as illustrated in Fig. 1B. As mentioned in main text, we adopt a parameter "*inhomogeneity*" of Jones matrix, i.e. the inner product of two eigen-states $\boldsymbol{\eta} = \langle \zeta_1 | \zeta_2 \rangle$. The amplitude of this parameter not only describes the degree of inhomogeneity of Jones matrix, but also provides an intuitive geometric standard for parallelism of the eigen-vectors on Poincaré sphere. Based on the Jones variables of two eigen-states, the degree of inhomogeneity can be expressed by:

$$|\boldsymbol{\eta}| = \cos^2(\alpha_1 - \alpha_2)\cos^2\left(\frac{\beta_2 - \beta_1}{2}\right) + \cos^2(\alpha_1 + \alpha_2)\sin^2\left(\frac{\beta_2 - \beta_1}{2}\right) \tag{S7}$$

We see that the inhomogeneity of Jones matrix is relative to dual eigen-states that can be inherently tailored by the geometric stacked configuration of the proposed meta-atom, which will be analyzed in the following sections.

1.3 Spectrum theorem and biorthogonal analyses of non-Hermitian Jones matrix

To explore the effects of orthogonality of eigen-states on polarizing behaviors, here we exploit the spectrum theorem to express the Jones matrix within an intuitive form. For a two-dimensional polarizing element owning orthogonal eigen-states ($|\boldsymbol{\eta}| = 0$), such as conventional single layered device like retarders and polarizers, the spectrum expansion of its Jones matrix $\boldsymbol{J}$ is described as[S1, S2]:

$$\boldsymbol{J} = \sum_{j=1}^{2}\sum_{i=1}^{2} \langle \zeta_i | \boldsymbol{J} | \zeta_j \rangle |\zeta_i\rangle\langle\zeta_j| = \boldsymbol{\kappa}_1 |\zeta_1\rangle\langle\zeta_1| + \boldsymbol{\kappa}_2 |\zeta_2\rangle\langle\zeta_2| \tag{S8}$$

Such operator is normal and only adapts to some basic birefringent devices in their eigen-formalism. For polarizing operators with non-orthogonal eigen-states ($|\eta| > 0$), Eq. (S8) does not work anymore due to the mutual coupling between the non-orthogonal vector directions. Thus, the biorthogonal analyses should be applied to manage this non-normal device operators. As introduced above, the eigen-vectors of general non-Hermitian matrix are represented by $|\zeta_{1,2}\rangle$. Here we associate another two reciprocal vectors $|\xi_{1,2}\rangle$, which satisfy the following condition:

$$\langle \xi_i | \zeta_j \rangle = \delta_{mn} = \begin{cases} 1, i = j \\ 0, i \neq j \end{cases}, i, j = 1, 2 \tag{S9}$$

It is noted that both eigen-state pairs $|\zeta_{1,2}\rangle$ and $|\xi_{1,2}\rangle$ constitute the biorthogonal eigen-system of the non-orthogonal polarizing operators. According to Eq. (S9), the expressions of associate vectors $|\xi_{1,2}\rangle$ are derived as:

$$\begin{cases} \left|\xi_1\right\rangle = \dfrac{e^{i\angle\eta}}{\sqrt{1-|\eta|^2}}\left|\zeta_2^{\perp}\right\rangle \\ \left|\xi_2\right\rangle = \dfrac{e^{-i\angle\eta}}{\sqrt{1-|\eta|^2}}\left|\zeta_1^{\perp}\right\rangle \end{cases} \tag{S10}$$

where $\left\langle\zeta_i^{\perp}\middle|\zeta_i\right\rangle = 0, i = 1,2$. Based on Eq. (S10), the spectrum expansion of non-orthogonal polarizing element can be presented in a general form:

$$\boldsymbol{J} = \boldsymbol{\kappa}_1 \frac{e^{-i\angle\boldsymbol{\eta}}}{\sqrt{1-|\boldsymbol{\eta}|^2}}\left|\zeta_1\right\rangle\left\langle\zeta_2^{\perp}\right| + \boldsymbol{\kappa}_2 \frac{e^{i\angle\boldsymbol{\eta}}}{\sqrt{1-|\boldsymbol{\eta}|^2}}\left|\zeta_2\right\rangle\left\langle\zeta_1^{\perp}\right| \tag{S11}$$

Thus, this formula is intuitive to express the non-orthogonal eigen-mode of polarizing devices and convenient to analyze the polarization transformation efficiency.

Note 2. Numerical calculations on efficiency limit of arbitrary polarization transformations

To theoretically prove the efficiency limit of arbitrary polarization transformation, we perform calculations based on physically achievable Jones matrices to obtain all possible input-output state transformations in the entire polarization space.

Firstly, we establish a library of Jones matrices with assigned complex values, whose real and imaginary parts of four coefficients J_{xx}, J_{xy}, J_{yx}, J_{yy} are uniformly sampled from -1 to1 with a step of 0.2. On this basis, by exploiting the strict condition of orthogonality $|\boldsymbol{\eta}|=0$ on the eigen-states of the Jones matrices, we classify them into orthogonal and non-orthogonal types, as illustrated in main text.

Secondly, to quantitatively analyze the polarization transformation performances, we sample 2601 points that uniformly covering the whole polarization space as the presetting standards. When the input polarization is randomly fixed (here we take $\left|\vec{\boldsymbol{E}}^{in}\right\rangle = \begin{bmatrix} \cos\alpha^{in} \\ \sin\alpha^{in}\cdot e^{i\beta^{in}} \end{bmatrix}, \begin{cases} \alpha^{in} = \pi/4 \\ \beta^{in} = 3\pi/5 \end{cases}$ as an example), all the possible transformed output polarization states that infinitely close to presetting points can be obtained through Jones matrices library ($\left|\vec{\boldsymbol{E}}^{out}\right\rangle = \boldsymbol{J}\left|\vec{\boldsymbol{E}}^{in}\right\rangle$). Here we set error threshold of elliptical angle and declination angle as 0.015 (rad, for α) and 0.05 (rad, for β) for demarcating the generated output states. The output states obtained from orthogonal and non-orthogonal Jones matrices are illustrated on the Poincaré sphere, respectively (Figs. S1A and S1B). For the orthogonal Jones matrices with such assignment accuracy eigen-bases, the preset input state cannot be transformed into the all-possible outputs covering the entire polarization space (only 1034 output states), indicating the arbitrariness of polarization transformation is physically limited. Nevertheless, under the non-orthogonal eigen-bases with same assignment accuracy, all desired 2601 polarization states can be achieved from the preset input state.

Then, the efficiencies of the corresponding input-output polarization transformation processes are calculated ($T = \dfrac{\left\langle \vec{\boldsymbol{E}}^{out} \middle| \vec{\boldsymbol{E}}^{out} \right\rangle}{\left\langle \vec{\boldsymbol{E}}^{in} \middle| \vec{\boldsymbol{E}}^{in} \right\rangle} = \dfrac{\left\langle \vec{\boldsymbol{E}}^{in} \middle| \boldsymbol{J}^{\dagger}\boldsymbol{J} \middle| \vec{\boldsymbol{E}}^{in} \right\rangle}{\left\langle \vec{\boldsymbol{E}}^{in} \middle| \vec{\boldsymbol{E}}^{in} \right\rangle}$) and displayed in Figs. S1C and S1D. We see that the transformation efficiencies of all the output states based on orthogonal Jones matrices are distributed between (0,1) while the efficiencies calculated by non-orthogonal Jones matrices can be enhanced and approaching to the unity. To further evaluate the polarizing modulation abilities of orthogonal and non-orthogonal eigen-bases, we introduce the concept of coverage ratio $R = \dfrac{N_{eff}}{N_{pre}}$ under a specific preset efficiency threshold, where N_{eff} is the number of distinguished outputs with efficiency over the preset threshold, while N_{pre} denotes the total number of presetting output states (2601 in this work). Calculated R against the efficiency threshold is displayed in main text (Fig. 1C). It is seen that when the efficiency threshold is 0 (without any constrain on the polarization conversion efficiency), R under orthogonal eigen-base is 0.4 while that of non-orthogonal case is close to unity. When the efficiency threshold increases to 0.9, the coverage ratios of orthogonal and non-orthogonal are 0.1 and 0.99, respectively. Such comparison in coverage ratios of output states not only proves the absolute arbitrariness in polarization transformation of non-orthogonal eigen-bases, but also indicates the corresponding extremely high efficiency performances.

Lastly, for considering the all-possible input-output transformation situations, we set input polarizations as arbitrary states covering the entire polarization space to show the generality, as $\left|\vec{\boldsymbol{E}}^{in}\right\rangle=\begin{bmatrix}\cos\alpha^{in}\\ \sin\alpha^{in}\cdot e^{i\beta^{in}}\end{bmatrix},\begin{cases}\alpha^{in}\in[0,\pi/2]\\ \beta^{in}\in[-\pi,\pi]\end{cases}$, where the sampling interval is set as $\pi/20$. When the efficiency threshold is fixed to 0.9, the coverage ratios obtained under variable input states are displayed in Fig. 1D in main text. It is observed that all the output polarization states can be high-efficiently achieved under arbitrary input state based on the non-orthogonal eigen-bases. Such results powerfully elucidate that the orthogonality between two eigen-states of Jones matrices is the physical limitation on the arbitrariness and efficiency of the random polarization transformations. Once the orthogonality restriction is unlocked, any input-output transformation can be physically achieved with extremely high efficiencies.

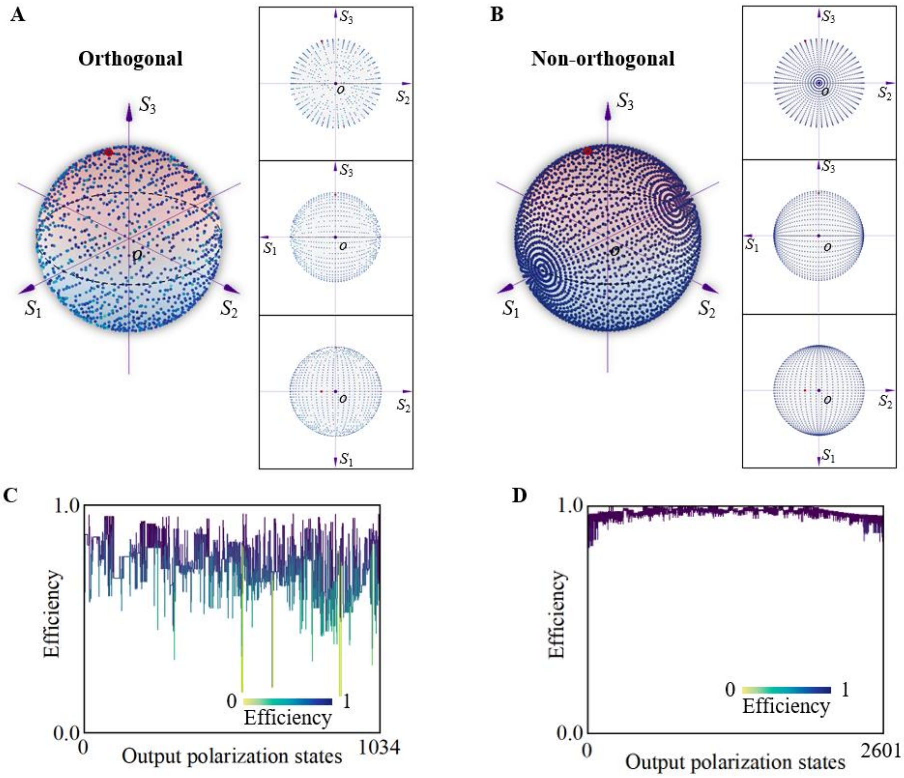

Fig. S1 All the output polarization states transformed from the presetting input state (red point on the Poincaré sphere) with (A) orthogonal and (B) non-orthogonal eigen polarization states, the insets show the different plane perspectives from axes S_1, S_2, S_3, respectively. Efficiencies of all possible input-output polarization transformations obtained from (C) orthogonal and (D) non-orthogonal eigen polarization states.

Note 3. Theoretical model of wave matrix for non-orthogonal meta-structure analyses

Firstly, we propose a multilayered structure of interval placed n^{th} metallic layers and $(n+1)^{\text{th}}$ dielectric layers with wave impedance $\eta_n = \sqrt{\mu_n/\varepsilon_n}$, as shown in Fig. S2. Such a structure can be regarded as a four-port cascading network whose input and terminating ports are the 1^{st} and $(n+1)^{\text{th}}$ dielectric layers. Here, we suppose that a plane wave propagates along +z-axis and the electric field is distributed in xoy plane. As for the n^{th} dielectric spacer, the total electric field is presented as $\vec{\boldsymbol{E}}_n = \vec{\boldsymbol{E}}_n^+ + \vec{\boldsymbol{E}}_n^-$, where $\vec{\boldsymbol{E}}_n^+ = \begin{bmatrix} E_{nx}^+ \\ E_{ny}^+ \end{bmatrix}$ and $\vec{\boldsymbol{E}}_n^- = \begin{bmatrix} E_{nx}^- \\ E_{ny}^- \end{bmatrix}$ are the forward and backward electric field, respectively. Meanwhile, the corresponding magnetic fields are calculated by $\vec{\boldsymbol{H}}_n^+ = \dfrac{\boldsymbol{n}}{\eta_n}\vec{\boldsymbol{E}}_n^+$ and $\vec{\boldsymbol{H}}_n^- = -\dfrac{\boldsymbol{n}}{\eta_n}\vec{\boldsymbol{E}}_n^-$ (where $\boldsymbol{n} = \begin{bmatrix} 0 & -1 \\ 1 & 0 \end{bmatrix}$ is the rotation matrix). For simplicity, we just consider the electric field transformation relationship in the stacked structure, which is quite suitable to calculate scattering parameters and wave matrix transformation process. Scattering parameters $S = \begin{bmatrix} \boldsymbol{S}_{11} & \boldsymbol{S}_{12} \\ \boldsymbol{S}_{21} & \boldsymbol{S}_{22} \end{bmatrix}$ (S-matrix) describe the transmission relationship between input and output electric fields relative to the metallic layer separating n^{th} and $(n+1)^{th}$ dielectric layers, which can be expressed by $\begin{bmatrix} \vec{E}_n^- \\ \vec{E}_{n+1}^+ \end{bmatrix} = \begin{bmatrix} \boldsymbol{S}_{11} & \boldsymbol{S}_{12} \\ \boldsymbol{S}_{21} & \boldsymbol{S}_{22} \end{bmatrix} \begin{bmatrix} \vec{E}_n^+ \\ \vec{E}_{n+1}^- \end{bmatrix}$ and unfolded as:

$$\begin{bmatrix} E_{nx}^- \\ E_{ny}^- \\ E_{(n+1)x}^+ \\ E_{(n+1)y}^+ \end{bmatrix} = \begin{bmatrix} S_{11}^{xx} & S_{11}^{xy} & S_{12}^{xx} & S_{12}^{xy} \\ S_{11}^{yx} & S_{11}^{yy} & S_{12}^{yx} & S_{12}^{yy} \\ S_{21}^{xx} & S_{21}^{xy} & S_{22}^{xx} & S_{22}^{xy} \\ S_{21}^{yx} & S_{21}^{yy} & S_{22}^{yx} & S_{22}^{yy} \end{bmatrix} \begin{bmatrix} E_{nx}^+ \\ E_{ny}^+ \\ E_{(n+1)x}^- \\ E_{(n+1)y}^- \end{bmatrix} \tag{S12}$$

where the subscripts "1" and "2" in 4 × 4 complex S-matrix present the output and input ports, and the superscripts show the linear polarization state of the output and input ports, respectively. However, it is easy to find that S-matrix cannot be directly multiplied for cascading models. On another hand, the wave matrix $M = \begin{bmatrix} \boldsymbol{M}_{11} & \boldsymbol{M}_{12} \\ \boldsymbol{M}_{21} & \boldsymbol{M}_{22} \end{bmatrix}$ connects the forward and backward electric field directly, shown as $\begin{bmatrix} \vec{E}_n^+ \\ \vec{E}_n^- \end{bmatrix} = \begin{bmatrix} \boldsymbol{M}_{11} & \boldsymbol{M}_{12} \\ \boldsymbol{M}_{21} & \boldsymbol{M}_{22} \end{bmatrix} \begin{bmatrix} \vec{E}_{n+1}^+ \\ \vec{E}_{n+1}^- \end{bmatrix}$ and unfolded as:

$$
\begin{bmatrix} E_{nx}^{+} \\ E_{ny}^{+} \\ E_{nx}^{-} \\ E_{ny}^{-} \end{bmatrix} = \begin{bmatrix} M_{11}^{xx} & M_{11}^{xy} & M_{12}^{xx} & M_{12}^{xy} \\ M_{11}^{yx} & M_{11}^{yy} & M_{12}^{yx} & M_{12}^{yy} \\ M_{21}^{xx} & M_{21}^{xy} & M_{22}^{xx} & M_{22}^{xy} \\ M_{21}^{yx} & M_{21}^{yy} & M_{22}^{yx} & M_{22}^{yy} \end{bmatrix} \begin{bmatrix} E_{(n+1)x}^{+} \\ E_{(n+1)y}^{+} \\ E_{(n+1)x}^{-} \\ E_{(n+1)y}^{-} \end{bmatrix} \tag{S13}
$$

Based on Eqs. (S12) and (S13), we can obtain the transformation relationship between S-matrix and wave matrix, which is expressed by:

$$
\begin{aligned}
\boldsymbol{M} &= \begin{bmatrix} \boldsymbol{I} & \boldsymbol{0} \\ \boldsymbol{S}_{11} & \boldsymbol{S}_{12} \end{bmatrix} \begin{bmatrix} \boldsymbol{S}_{21} & \boldsymbol{S}_{22} \\ \boldsymbol{0} & \boldsymbol{I} \end{bmatrix}^{-1} \\
&= \frac{1}{S_{21}^{xx}S_{21}^{yy} - S_{21}^{xy}S_{21}^{yx}} \begin{bmatrix}
S_{21}^{yy} & -S_{21}^{xy} & S_{21}^{xy}S_{22}^{yx} - S_{21}^{yy}S_{22}^{xx} & S_{21}^{xy}S_{22}^{yy} - S_{21}^{yy}S_{22}^{xy} \\
-S_{21}^{yx} & -S_{21}^{xx} & -S_{21}^{xx}S_{22}^{yx} + S_{21}^{yx}S_{22}^{xx} & -S_{21}^{xx}S_{22}^{yy} + S_{21}^{yx}S_{22}^{xy} \\
S_{11}^{xx}S_{21}^{yy} - S_{11}^{xy}S_{21}^{yx} & S_{11}^{xy}S_{21}^{xx} - S_{11}^{xx}S_{21}^{xy} & \begin{array}{c} S_{12}^{xx}\left(S_{21}^{xx}S_{21}^{yy} - S_{21}^{xy}S_{21}^{yx}\right) \\ -S_{11}^{xy}\left(S_{21}^{xx}S_{22}^{yx} - S_{21}^{yx}S_{22}^{xx}\right) \\ +S_{11}^{xx}\left(S_{21}^{xy}S_{22}^{yx} - S_{21}^{yy}S_{22}^{xx}\right) \end{array} & \begin{array}{c} S_{12}^{xy}\left(S_{21}^{xx}S_{21}^{yy} - S_{21}^{xy}S_{21}^{yx}\right) \\ -S_{11}^{xy}\left(S_{21}^{xx}S_{22}^{yy} - S_{21}^{yx}S_{21}^{xy}\right) \\ +S_{12}^{xx}\left(S_{21}^{xy}S_{22}^{yy} - S_{22}^{yy}S_{21}^{xy}\right) \end{array} \\
S_{11}^{yx}S_{21}^{yy} - S_{11}^{yy}S_{21}^{yx} & S_{11}^{yy}S_{21}^{xx} - S_{11}^{yx}S_{21}^{xy} & \begin{array}{c} S_{12}^{yx}\left(S_{21}^{xx}S_{21}^{yy} - S_{21}^{xy}S_{21}^{yx}\right) \\ -S_{11}^{yy}\left(S_{21}^{xx}S_{22}^{yx} - S_{21}^{yx}S_{22}^{xx}\right) \\ +S_{11}^{yx}\left(S_{21}^{xy}S_{22}^{yx} - S_{21}^{yy}S_{22}^{xx}\right) \end{array} & \begin{array}{c} S_{12}^{yy}\left(S_{21}^{xx}S_{21}^{yy} - S_{21}^{xy}S_{21}^{yx}\right) \\ -S_{11}^{yy}\left(S_{21}^{xx}S_{22}^{yy} - S_{21}^{yx}S_{21}^{xy}\right) \\ +S_{12}^{yx}\left(S_{21}^{xy}S_{22}^{yy} - S_{22}^{yy}S_{21}^{xy}\right) \end{array}
\end{bmatrix}
\end{aligned} \tag{S14}
$$

Once S-matrix of any meta-atom is attained, its wave matrix can be derived by Eq. (S14). Meanwhile, S-matrix can also be obtained by the fixed wave matrix information:

$$
\begin{aligned}
\boldsymbol{S} &= \begin{bmatrix} \boldsymbol{0} & \boldsymbol{M}_{11} \\ -\boldsymbol{I} & \boldsymbol{M}_{21} \end{bmatrix}^{-1} \begin{bmatrix} \boldsymbol{I} & -\boldsymbol{M}_{12} \\ \boldsymbol{0} & -\boldsymbol{M}_{22} \end{bmatrix} \\
&= \frac{1}{M_{11}^{xx}M_{11}^{yy} - M_{11}^{xy}M_{11}^{yx}} \begin{bmatrix}
\begin{array}{c} -M_{11}^{yx}M_{21}^{xy} \\ +M_{11}^{yy}M_{21}^{xx} \end{array} & \begin{array}{c} M_{11}^{xx}M_{21}^{xy} \\ -M_{11}^{xy}M_{21}^{xx} \end{array} & \begin{array}{c} M_{22}^{xx}\left(M_{11}^{xx}M_{11}^{yy} - M_{11}^{xy}M_{11}^{yx}\right) \\ -M_{12}^{yx}\left(M_{11}^{xx}M_{21}^{xy} - M_{11}^{xy}M_{21}^{xx}\right) \\ +M_{12}^{xx}\left(M_{11}^{yx}M_{21}^{xy} - M_{11}^{yy}M_{21}^{xx}\right) \end{array} & \begin{array}{c} M_{22}^{xy}\left(M_{11}^{xx}M_{11}^{yy} - M_{11}^{xy}M_{11}^{yx}\right) \\ -M_{12}^{yy}\left(M_{11}^{xx}M_{21}^{xy} - M_{11}^{xy}M_{21}^{xx}\right) \\ +M_{12}^{xy}\left(M_{11}^{yx}M_{21}^{xy} - M_{11}^{yy}M_{21}^{xx}\right) \end{array} \\
\begin{array}{c} -M_{11}^{yx}M_{21}^{yy} \\ +M_{11}^{yy}M_{21}^{yx} \end{array} & \begin{array}{c} M_{11}^{xx}M_{21}^{yy} \\ -M_{11}^{xy}M_{21}^{yx} \end{array} & \begin{array}{c} M_{22}^{yx}\left(M_{11}^{xx}M_{11}^{yy} - M_{11}^{xy}M_{11}^{yx}\right) \\ -M_{12}^{yx}\left(M_{11}^{xx}M_{21}^{yy} - M_{11}^{xy}M_{21}^{yx}\right) \\ +M_{12}^{xx}\left(M_{11}^{yx}M_{21}^{yy} - M_{11}^{yy}M_{21}^{yx}\right) \end{array} & \begin{array}{c} M_{22}^{yy}\left(M_{11}^{xx}M_{11}^{yy} - M_{11}^{xy}M_{11}^{yx}\right) \\ -M_{12}^{yy}\left(M_{11}^{xx}M_{21}^{yy} - M_{11}^{xy}M_{21}^{yx}\right) \\ +M_{12}^{xy}\left(M_{11}^{yx}M_{21}^{yy} - M_{11}^{yy}M_{21}^{yx}\right) \end{array} \\
M_{11}^{yy} & -M_{11}^{xy} & M_{11}^{xy}M_{12}^{yx} - M_{11}^{yy}M_{12}^{xx} & M_{11}^{xy}M_{12}^{yy} - M_{11}^{yy}M_{12}^{xy} \\
-M_{11}^{yyx} & M_{11}^{xx} & M_{11}^{yx}M_{12}^{xx} - M_{11}^{xx}M_{12}^{yx} & M_{11}^{yx}M_{12}^{xy} - M_{11}^{xx}M_{12}^{yy}
\end{bmatrix}
\end{aligned} \tag{S15}
$$

Considering the stacked model calculation illustrated in Fig. S2, we further discuss the rotation function of the metallic layers (with rotated θ), which can be described by a 4 × 4 rotation matrix as $\boldsymbol{P}(\theta) = \boldsymbol{I} \otimes \boldsymbol{R}(\theta)$ and expanded under the Kronecker tensor product effect:

$$R(\theta)=\begin{bmatrix}1 & 0\\ 0 & 1\end{bmatrix}\otimes\begin{bmatrix}\cos\theta & -\sin\theta\\ \sin\theta & \cos\theta\end{bmatrix}=\begin{bmatrix}\cos\theta & -\sin\theta & 0 & 0\\ \sin\theta & \cos\theta & 0 & 0\\ 0 & 0 & \cos\theta & -\sin\theta\\ 0 & 0 & \sin\theta & \cos\theta\end{bmatrix} \tag{S16}$$

We define the wave matrix of n^{th} metallic layer as $\boldsymbol{M_n}$, which is labelled as $M_n^{rot}=R(\theta_j)M_nR(\theta_j)^T$ with the rotation angle θ_j, while that of n^{th} dielectric layer is $\boldsymbol{M_{dn}}$. According to the definition of wave matrix, we can obtain the whole wave matrix of the stacked model by directly multiplying that of each component:

$$M_{tot}=M_{d1}M_1^{rot}M_{d2}M_2^{rot}\cdots M_{n-1}^{rot}M_{dn}M_n^{rot}M_{d(n+1)} \tag{S17}$$

Then, S-matrix of this stacked model can be obtained through substituting Eq. (S17) into Eq. (S15).

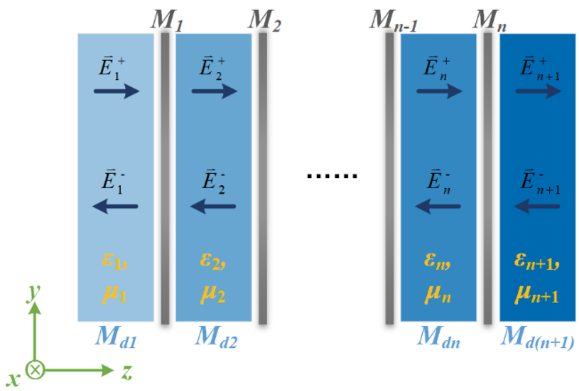

Fig. S2 Schematic of cascading model with multiple metallic and dielectric layers.

Note 4. Mechanism of the proposed non-orthogonal meta-atom

To achieve the inhomogeneous Jones matrix with dual unrestricted eigen-states, we exploit a multilayered meta-atom with chirality configuration by twisting the relative rotation offset between different functional components. Such meta-structures have been widely studied for its famous circular dichroism performances[S3-S6]. However, the properties of non-orthogonal eigen-states have not been studied in deep yet. Applying the theoretical cascading network model as illustrated in Fig. S2, we can analytically characterize the contribution of geometric parameters to inhomogeneous Jones matrix. Due to mature fabrication technology in microwave region, *i.e.*, printed circuit board (PCB) and multilayer pressing technology, we design a stacking-twisted meta-atom, namely "*non-orthogonal*" meta-atom (Fig. 2A in main text) composed of three metallic rectangular patch elements, two metallic grid elements, interleaved with four dielectric substrates. The functional elements are the rectangular patches with three parallel gaps that create the miniaturization condition for meta-atom sizes. The width and length of the rectangular patch is labelled as p_x and p_y, the gaps width and length are $w_x = 0.5p_x$ and $w_y = 0.17p_y$, and the relative distance between adjacent gaps is $g = 0.25p_y$. All these five parameters provide tailoring possibility for amplitude and phase profiles of two eigen-values of corresponding non-Hermitian Jones matrix. Three patch elements with same configuration but different rotation angles θ_1, θ_2, and θ_3 are the key factor to break the construction symmetries and realize the inhomogeneous Jones matrix with non-orthogonal eigen-states. As for sandwiched dielectric layer and metallic grid layer, we design a grid component with circle aperture to be insensitive for patch elements rotations, and the radius of circle aperture is r = 4.5 mm. Meanwhile, four dielectric substrates have same material parameters with permittivity $\varepsilon_r = 3.5$ and thickness h = 1 mm. From the view of equivalent circuit model, this multi-layered meta-atom can provide a band-pass non-resonant profile within the target bandwidth. Thereinto, three rectangular patches act as the capacitance elements, two grid layers are inductance elements, and four dielectric substrates are equivalent to transmission lines in such cascading network. Thus, the meta-atom model can be regarded as a multi-order bandpass filter network. The specific explanations can be found in our previous work[S10].

Then, we adopt the wave matrix detailed in Note 3 to construct the theoretical model of the proposed non-orthogonal meta-atom to explicitly show the inhomogeneity effect of Jones matrix. Firstly, we can obtain the scattering parameters of each single layer in meta-atom through the full-wave simulations. Due to the in-plane symmetry, passive, and reciprocity conditions of j^{th} (j = 1, 2, 3) rectangular patch components, we can obtain $S^{xy} = S^{yx} = 0$, and $\boldsymbol{S_{11}} = \boldsymbol{S_{22}}$, $\boldsymbol{S_{12}} = \boldsymbol{S_{21}}$. Thus, the scattering parameters of single patch component can be simplified as:

$$\boldsymbol{S}_{patch-j} = \begin{bmatrix} S_{11}^{xx} & 0 & S_{12}^{xx} & 0 \\ 0 & S_{11}^{yy} & 0 & S_{12}^{yy} \\ S_{21}^{xx} & 0 & S_{22}^{xx} & 0 \\ 0 & S_{21}^{yy} & 0 & S_{22}^{yy} \end{bmatrix} \tag{S18}$$

Figs. S3 – S5 display the simulated scattering parameters of each single n^{th} ($n = 1, 2, 3$) rectangular patch with variable p_x and p_y changing from 1.5 mm to 8.5 mm, whose rotation angles are set as $\theta_1 = 0°$, $\theta_2 = 30°$, $\theta_3 = 75°$, respectively. The up-right corners in all the mapping of different scattering responses are all with null data due to the invalid rectangular patches whose diagonal length are larger than the periodic size $a = 10$ mm. We can observe that the scattering responses at working frequency 10 GHz of single patch obviously vary with its geometric sizes. When the patch layer undergoes no rotation, the cross-polarized components present all zero profiles with disordered phase responses. With the rotation angle increasing, the amplitudes of cross-polarized components get larger than 0 and the corresponding phase responses exhibit obvious tendency with variable sizes, instead of disordered . Meanwhile, the phase coverage in each linearly polarized scattering coefficient of single patch is far less than 2π no matter the rotation angle, which also is one of the impetuses to explore stacked meta-structures carrying extra degrees of freedom (DOFs) and full phase coverage. Additionally, the same variable tendency appears in reflection coefficients from different ports $\boldsymbol{S_{11}}$ and $\boldsymbol{S_{22}}$, transmission coefficients $\boldsymbol{S_{12}}$ and $\boldsymbol{S_{21}}$, indicating that the reciprocal performance of single-layered patches is insensitive to rotation angles. In the full wave simulation, different patches are set with distinct surroundings and specific boundary conditions, according to the corresponding position in cascading model. Table S1 displays the background material settings of input and output circumstances. As for subsequent cascading calculation, the inverse wave matrices of input vacuum space and output dielectric space are multiplied in order to obtain the pure wave matrix of single patch as in simulation model.

It is worth noting that the distance between adjacent metallic components is much smaller than working wavelength in our scenario. Therefore, there inevitably exists coupling effect in the cascading meta-atom configuration. The proposed layer-by-layer analysis in the cascading meta-atom aims to precisely ascertain the physical effect of interlaminated rotation offsets on chirality performances and further on the non-orthogonal eigen-states. Hence, we just contribute the coupling effect between the grid and patch to be a part of the scattering performance of grid component in the wave matrix, instead of offering formula to analytically characterize it. Comparing the simulated S parameters of single patch model (Σ_{patch}) and patch-substrate-grid (Σ_{PSG}) model, whose calculated wave matrices are M_{patch} and M_{PSG}, respectively, the wave matrix of grid combined with interlayered coupling effect M_{grid} can be expressed by $\boldsymbol{M}_{grid} = \boldsymbol{M}_{patch}^{-1}\boldsymbol{M}_{die}^{-1}\boldsymbol{M}_{PSG}$, where M_{die} is wave matrix of dielectric substrate located between patch and grid components in patch-substrate-grid model and fixed at the specific wavelength due to the invariable material parameters. Based on such operation, the coupling effect is integrated into the wave matrix of metallic grids, which can be directly multiplied and operated in the whole cascading meta-atom construction.

Next, based on the above simulation and analyses verification of scattering responses of each component in proposed meta-atom, we transform scattering parameters into corresponding wave matrix and multiply separate wave matrices in the cascading order to obtain the whole stacked meta-structure. Here the wave matrix of n^{th} (n = 1, 2, 3) patch with rotation angle θ_n can be expressed as:

$$\begin{aligned}
\boldsymbol{M}_{patch-n}^{rot} &= \boldsymbol{R}(\theta_n)\boldsymbol{M}_{patch-n}\boldsymbol{R}(\theta_n)^{\mathrm{T}} \\
&= \boldsymbol{R}(\theta_n)\begin{bmatrix} \frac{1}{S_{21}^{xx}} & 0 & \frac{S_{22}^{xx}}{S_{21}^{xx}} & 0 \\ 0 & \frac{1}{S_{21}^{yy}} & 0 & \frac{S_{22}^{yy}}{S_{21}^{yy}} \\ \frac{S_{11}^{xx}}{S_{21}^{xx}} & 0 & \frac{S_{11}^{xx}S_{22}^{xx}+S_{21}^{xx}S_{12}^{xx}}{S_{21}^{xx}} & 0 \\ 0 & \frac{S_{11}^{yy}}{S_{21}^{yy}} & 0 & \frac{S_{11}^{yy}S_{22}^{yy}+S_{21}^{yy}S_{12}^{yy}}{S_{21}^{xx}} \end{bmatrix}\boldsymbol{R}(\theta_n)^{\mathrm{T}} \\
&= \boldsymbol{M}_a \otimes \boldsymbol{I} + \boldsymbol{M}_b \otimes \boldsymbol{R}'
\end{aligned} \tag{S19}$$

where $\boldsymbol{R}'(\theta_n) = \begin{bmatrix} \cos(2\theta_n) & \sin(2\theta_n) \\ \sin(2\theta_n) & -\cos(2\theta_n) \end{bmatrix}$ is a rotation factor, and $\boldsymbol{M}_{a,b}$ are two complex matrix in term of scattering parameters of single patch that are only affected by p_x and p_y, shown as:

$$\boldsymbol{M}_a = \frac{1}{2}\begin{bmatrix} \frac{1}{S_{21}^{xx}} + \frac{1}{S_{21}^{yy}} & \frac{S_{22}^{xx}}{S_{21}^{xx}} + \frac{S_{22}^{yy}}{S_{21}^{yy}} \\ \frac{S_{11}^{xx}}{S_{21}^{xx}} + \frac{S_{11}^{yy}}{S_{21}^{yy}} & \frac{S_{11}^{xx}S_{22}^{xx}+S_{21}^{xx}S_{12}^{xx}}{S_{21}^{xx}} + \frac{S_{11}^{yy}S_{22}^{yy}+S_{21}^{yy}S_{12}^{yy}}{S_{21}^{xx}} \end{bmatrix} \tag{S20a}$$

$$\boldsymbol{M}_b = \frac{1}{2}\begin{bmatrix} \frac{1}{S_{21}^{xx}} - \frac{1}{S_{21}^{yy}} & \frac{S_{22}^{xx}}{S_{21}^{xx}} - \frac{S_{22}^{yy}}{S_{21}^{yy}} \\ \frac{S_{11}^{xx}}{S_{21}^{xx}} - \frac{S_{11}^{yy}}{S_{21}^{yy}} & \frac{S_{11}^{xx}S_{22}^{xx}+S_{21}^{xx}S_{12}^{xx}}{S_{21}^{xx}} - \frac{S_{11}^{yy}S_{22}^{yy}+S_{21}^{yy}S_{12}^{yy}}{S_{21}^{xx}} \end{bmatrix} \tag{S20b}$$

As for the twisting configuration, the decisive factors are the rotation offsets between different patches in the meta-atom. The patch area $p_x \cdot p_y$, and aspect ratio p_y / p_x are the assisted factors for propagation phase responses manipulation. Thus, the multiplied wave matrix of the whole meta-atom is shown by:

$$\begin{aligned}
\boldsymbol{M}_{tot} = &\left(\boldsymbol{M}_a\right)^3 \otimes \mathbf{I} \\
&+\left[\left(\boldsymbol{M}_a\right)^2 \otimes \mathbf{I}\right] \cdot \left\{\boldsymbol{M}_b \otimes \left[\boldsymbol{R}'\left(\theta_1\right)+\boldsymbol{R}'\left(\theta_2\right)+\boldsymbol{R}'\left(\theta_3\right)\right]\right\} \\
&+\left(\boldsymbol{M}_a \otimes \mathbf{I}\right) \cdot \left\{\left(\boldsymbol{M}_b\right)^2 \otimes \left[\boldsymbol{R}'\left(\theta_1\right)\boldsymbol{R}'\left(\theta_2\right)+\boldsymbol{R}'\left(\theta_2\right)\boldsymbol{R}'\left(\theta_3\right)+\boldsymbol{R}'\left(\theta_1\right)\boldsymbol{R}'\left(\theta_3\right)\right]\right\} \\
&+\left(\boldsymbol{M}_b\right)^3 \otimes \boldsymbol{R}'\left(\theta_1\right)\boldsymbol{R}'\left(\theta_2\right)\boldsymbol{R}'\left(\theta_3\right)
\end{aligned} \tag{S21}$$

The scattering parameters of the whole meta-atom can be calculated through substituting Eq. (S21) into Eq. (S15). We just consider the transmission coefficients $\boldsymbol{S}_{21}$ of meta-atom in this work, which can be equivalent to the off-diagonal components in 4 × 4 scattering matrix as shown:

$$\begin{aligned}
\boldsymbol{S}_{21} &= \begin{bmatrix} \dfrac{M_{11}^{xx}}{M_{11}^{xx}M_{11}^{yy}-M_{11}^{xy}M_{11}^{yx}} & \dfrac{-M_{11}^{xy}}{M_{11}^{xx}M_{11}^{yy}-M_{11}^{xy}M_{11}^{yx}} \\ \dfrac{-M_{11}^{yx}}{M_{11}^{xx}M_{11}^{yy}-M_{11}^{xy}M_{11}^{yx}} & \dfrac{M_{11}^{yy}}{M_{11}^{xx}M_{11}^{yy}-M_{11}^{xy}M_{11}^{yx}} \end{bmatrix} \\
&= \mathrm{T}_1 \cdot \mathbf{I} + \mathrm{T}_3 \cdot \frac{e^{i2(\theta_1-\theta_2)}+e^{i2(\theta_1-\theta_3)}+e^{i2(\theta_2-\theta_3)}}{2} \cdot \begin{bmatrix} 1 & i \\ -i & 1 \end{bmatrix} \\
&+\mathrm{T}_3 \cdot \frac{e^{-i2(\theta_1-\theta_2)}+e^{-i2(\theta_1-\theta_3)}+e^{-i2(\theta_2-\theta_3)}}{2} \cdot \begin{bmatrix} 1 & -i \\ i & 1 \end{bmatrix} \\
&+\left(\mathrm{T}_2 \cdot \frac{e^{i2\theta_1}+e^{i2\theta_2}+e^{i2\theta_3}}{2} + \mathrm{T}_4 \cdot \frac{e^{i2(\theta_1-\theta_2+\theta_3)}}{2}\right) \cdot \begin{bmatrix} 1 & -i \\ -i & -1 \end{bmatrix} \\
&+\left(\mathrm{T}_2 \cdot \frac{e^{-i2\theta_1}+e^{-i2\theta_2}+e^{-i2\theta_3}}{2} + \mathrm{T}_4 \cdot \frac{e^{-i2(\theta_1-\theta_2+\theta_3)}}{2}\right) \cdot \begin{bmatrix} 1 & i \\ i & -1 \end{bmatrix}
\end{aligned} \tag{S22}$$

where T_i (i = 1, 2, 3, 4) can be expanded and expressed as:

$$\mathrm{T}_1 = \frac{\left(t_{xx}+t_{yy}\right)^3+\left(r_{xx}t_{xx}+r_{yy}t_{yy}\right)^2\left[t_{xx}\left(2+t_{xx}t_{yy}+r_{yy}^2\right)+t_{yy}\left(2+t_{xx}t_{yy}+r_{xx}^2\right)\right]}{8t_{xx}t_{yy}} \tag{S23a}$$

$$\mathrm{T}_2 = \frac{\left(t_{xx}-t_{yy}\right)\left[\left(t_{xx}+t_{yy}\right)^2+\left(r_{xx}t_{xx}+r_{yy}t_{yy}\right)^2\right]+\left(r_{xx}^2t_{xx}^2-r_{yy}^2t_{yy}^2\right)\left[t_{xx}\left(1+r_{yy}^2+t_{xx}t_{yy}\right)+t_{yy}\left(1+r_{xx}^2+t_{xx}t_{yy}\right)\right]}{8t_{xx}t_{yy}} \tag{S23b}$$

$$\mathrm{T}_3 = \frac{\left(t_{xx}+t_{yy}\right)\left[\left(t_{xx}-t_{yy}\right)^2+\left(r_{xx}t_{xx}+r_{yy}t_{yy}\right)^2\right]+\left(r_{xx}^2t_{xx}^2-r_{yy}^2t_{yy}^2\right)\left[t_{xx}\left(1-r_{yy}^2+t_{xx}t_{yy}\right)-t_{yy}\left(1-r_{xx}^2+t_{xx}t_{yy}\right)\right]}{8t_{xx}t_{yy}} \tag{S23c}$$

$$\mathrm{T}_4 = \frac{\left(t_{xx}-t_{yy}\right)^3+\left(r_{xx}t_{xx}-r_{yy}t_{yy}\right)^2\left[t_{xx}\left(2+t_{xx}t_{yy}-r_{yy}^2\right)-t_{yy}\left(2-t_{xx}t_{yy}-r_{xx}^2\right)\right]}{8t_{xx}t_{yy}} \tag{S23d}$$

Therefore, the Eq. (S22) can be simplified to:

$$\boldsymbol{J}=\begin{bmatrix} \mathrm{T}_1-\mathrm{T}_2\sum_{j=1}^{3}\cos(2\theta_j)+\mathrm{T}_3\sum_{j=1}^{3}\cos(2\Delta\theta_j)-\mathrm{T}_4\cos(2\theta_k) & \mathrm{T}_2\sum_{j=1}^{3}\sin(2\theta_j)+\mathrm{T}_3\sum_{j=1}^{3}\sin(2\Delta\theta_j)+\mathrm{T}_4\sin(2\theta_k) \\ -\mathrm{T}_2\sum_{j=1}^{3}\sin(2\theta_j)+\mathrm{T}_3\sum_{j=1}^{3}\sin(2\Delta\theta_j)-\mathrm{T}_4\sin(2\theta_k) & \mathrm{T}_1+\mathrm{T}_2\sum_{j=1}^{3}\cos(2\theta_j)+\mathrm{T}_3\sum_{j=1}^{3}\cos(2\Delta\theta_j)+\mathrm{T}_4\cos(2\theta_k) \end{bmatrix} \quad \text{(S24)}$$

For the sake of simplification, $\Delta\theta_j$ shows the rotation offsets between distinct patches, including θ_1 - θ_2, θ_1 - θ_3, and θ_2 - θ_3, while $\theta_k = \theta_1 - \theta_2 + \theta_3$. From the above analyses we can know that, independent responses in the four transmission coefficients can be attained by rotating three patches in meta-atom, which is the necessary condition to conduct the inhomogeneous Jones matrix with non-orthogonal eigen-states.

Furthermore, the corresponding eigen-values and eigen-states are derived as:

$$\left|\kappa_{1,2}\right\rangle = \mathrm{T}_1+\mathrm{T}_3\sum_{j=1}^{3}\cos(2\Delta\theta_j)\pm\boldsymbol{P} \quad \text{(S25a)}$$

$$\left|\zeta_{1,2}\right\rangle=\begin{bmatrix}\zeta_{1x,2x}\\ \zeta_{1y,2y}\end{bmatrix}\propto\begin{bmatrix} -\mathrm{T}_2\sum_{j=1}^{3}\cos(2\theta_j)-\mathrm{T}_4\cos(2\theta_k)\pm\boldsymbol{P} \\ -\mathrm{T}_2\sum_{j=1}^{3}\sin(2\theta_j)+\mathrm{T}_3\sum_{j=1}^{3}\sin(2\Delta\theta_j)-\mathrm{T}_4\sin(2\theta_k) \end{bmatrix} \quad \text{(S25b)}$$

where $\boldsymbol{P}=\sqrt{\mathrm{T}_2^{\,2}\sum_{j=1}^{3}\cos(4\theta_j)+\left(2\mathrm{T}_2^{\,2}+\mathrm{T}_3^{\,2}\right)\sum_{j=1}^{3}\cos(2\Delta\theta_j)+\mathrm{T}_3^{\,2}\cos(4\theta_k)+2\mathrm{T}_2\mathrm{T}_3\sum_{j=1}^{3}\cos2(\theta_j+\theta_k)}$ is the decoupling factor for eigen-value and eigen-states. It is noted that we display $\mathrm{T}_a = \mathrm{T}_2 / \mathrm{T}_1$, $\mathrm{T}_b = \mathrm{T}_3 / \mathrm{T}_1$, $\mathrm{T}_c = \mathrm{T}_4 / \mathrm{T}_1$ to present the normalized coefficients in Eq. (3) in main text.

Figs. S6A and S6B illustrate the amplitude and phase profiles of calculated scattering parameters based on above analyses and simulated scattering coefficients of the complete non-orthogonal meta-atom in CST software. The consistency between two sets of reflectance ($\boldsymbol{r} = \boldsymbol{S}_{11}$) and transmittance ($\boldsymbol{t} = \boldsymbol{S}_{21}$) curves indicates that the proposed analytical model can present the scattering responses of stacked meta-atom, which provides a prompt and direct method to predict the amplitude and phase response of stacking-twisted meta-atom for further establishing a complete library to prescribe the non-orthogonal eigen-states.

Fig. S7 displays real and imaginary parts of all four components of transmission coefficients t_{xx}, t_{xy}, t_{yx}, and t_{yy}. All real and imaginary components in Jones matrix of non-orthogonal meta-atom exhibit distinct responses at a specific meta-atom construction, and different output linear polarization responses change with variable rotation angles of rectangular patches. Such tunability provides a feasible strategy to achieve inhomogeneous Jones matrix in transmissive manner.

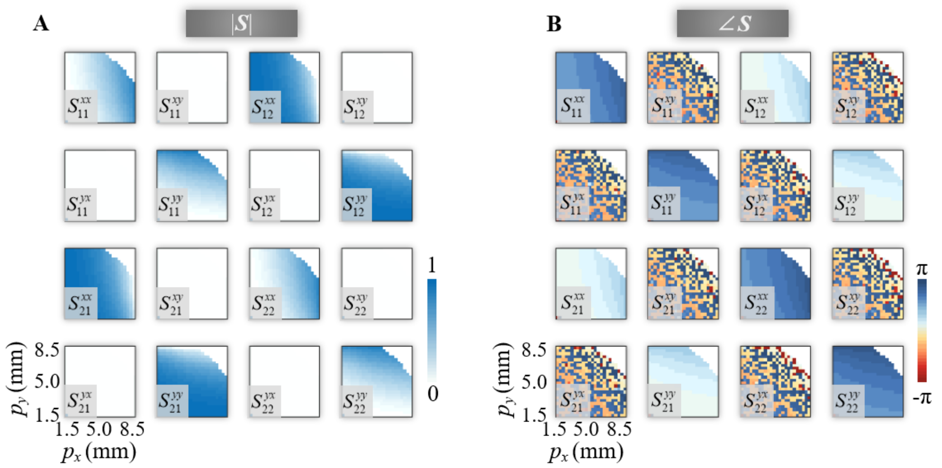

Fig. S3 Scattering parameters of 1[st] layered patch with rotation angle $\theta_1 = 0°$ against variable width and length sizes. (A) Amplitude and (B) phase profiles.

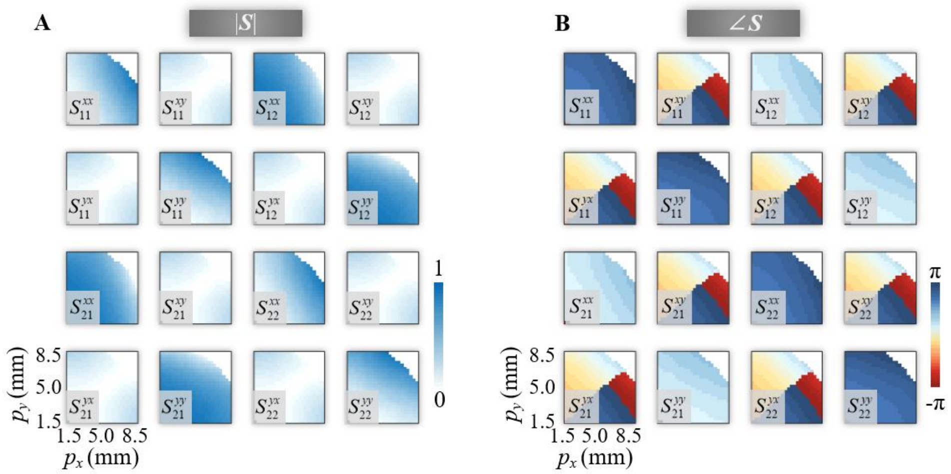

Fig. S4 Scattering parameters of 2[nd] layered patch with rotation angle $\theta_2 = 30°$ against variable width and length sizes. (A) Amplitude and (B) phase profiles.

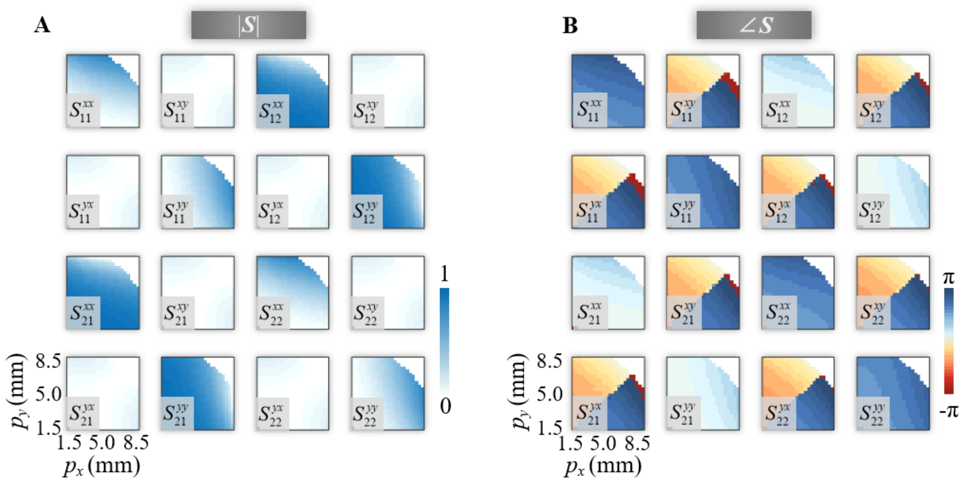

Fig. S5 Scattering parameters of 3[rd] layered patch with rotation angle $\theta_3 = 75°$ against variable width and length sizes. (A) Amplitude and (B) phase profiles.

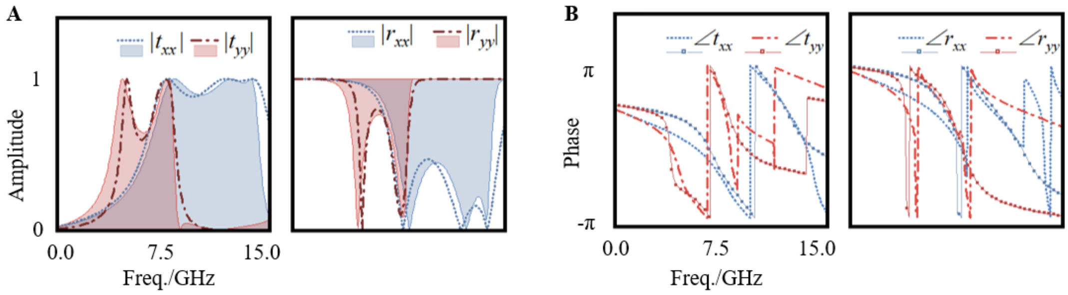

Fig. S6 Calculated and simulated (A) amplitude and (B) phase profiles of both transmittance ***t*** and reflectance coefficients ***r*** of the meta-atom, where dotted-lines denote calculated responses based on cascading wave matrix theory and filled area / symbolled line present simulated results.

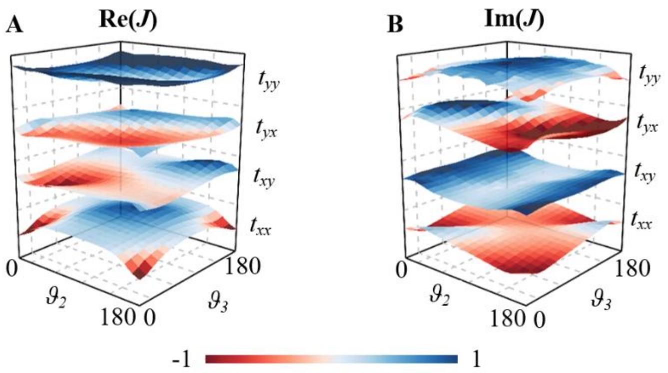

Fig. S7 (A) Real and (B) imaginary parts of four linearly polarized transmission coefficients in non-Hermitian Jones matrix against variable rotation of θ_2 and θ_3 (while $\theta_1 = 0$).

Table S1. Background settings in simulation of single patch component

	Input materials	**Output materials**
1st patch	Vacuum ($\varepsilon_{r\text{-}in} = 1$)	Dielectric Substrate ($\varepsilon_{r\text{-}out} = 3.5$)
2nd patch	Dielectric Substrate ($\varepsilon_{r\text{-}in} = 3.5$)	Dielectric Substrate ($\varepsilon_{r\text{-}out} = 3.5$)
3rd patch	Dielectric Substrate ($\varepsilon_{r\text{-}in} = 3.5$)	Vacuum ($\varepsilon_{r\text{-}out} = 1$)

Note 5. Analyses on stacking layers of meta-atom for inhomogeneity construction

The target of stacking meta-atom is to achieve full coverage of inhomogeneity degree [0, 1], which is theoretically guaranteed for complete spatial freedom of non-orthogonal eigen-state pair. Thus, we exploit $|\eta|$ as construction standard for minimum stacking number of functional elements.

5.1 Minimum stacking number of birefringent elements

Firstly, as for proposed multi-layered meta-atom configuration in main text, whose key elements are stacked three birefringent (rectangular) patches, we evaluate the degree of inhomogeneity as a function of functional patch number, as shown in Fig. S8. When meta-atom is designed with only one layer functional patch, as done with classical single-layer metasurface, the trajectories of Stokes eigen-states are related to each other by antipodal symmetry on Poincaré sphere, delineating the conventional case for homogeneous Jones matrix, as illustrated in the inset of Fig. S8A. Instead, for meta-atoms with more than one patches, by only rotating the bottom-layered patch from 0° to 180°, the distribution of eigen polarization pairs is not anymore symmetric with respect to the center of sphere, which provides a simple solution to address inhomogeneous Jones matrix. It is seen that $|\eta|$ can reach full coverage from 0 to 1 once the number of patch element approaches 3, with two dielectric-grid-dielectric interlayers acting as matching layer. Additionally, when 4 patches are stacked, inhomogeneity of [0, 1] can still be obtained. Thus, we choose to perform subsequent demonstrations on meta-atom with only 3 functional patch elements as sketched in Fig. 2A in main text, since more layers would unnecessarily increase the fabrication difficulties. Besides, we also explored the inhomogeneity performances of stacking anisotropic L-shaped elements, which are shown in Fig. S8B and the corresponding analyses exhibited in the next Note 5.2.

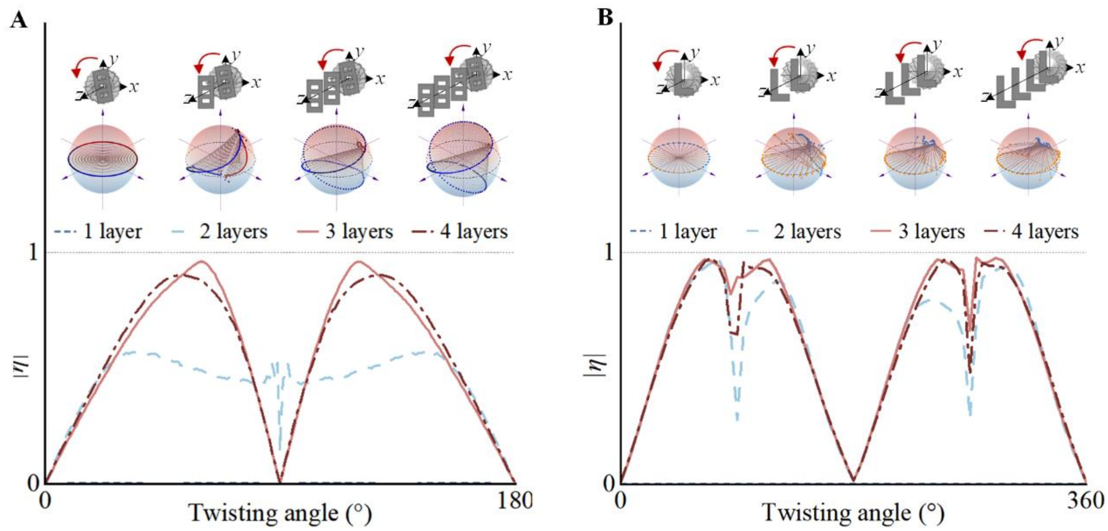

Fig. S8 (A) Degree of inhomogeneity of meta-atoms with different number of functional patch element(s) against θ_1 rotating from 0° to 180°. The inset shows simplified schematic of meta-atom with distinct patch elements, and the corresponding evolution trajectories of eigen-state pairs on Poincaré sphere. (B) Degree of inhomogeneity of meta-atoms with different number of functional L-shaped element(s) against rotating bottom layer from 0° to 360°. The inset shows simplified schematic of the meta-atom with distinct L-shaped elements, and the corresponding evolution trajectories of the eigen-state pairs on the Poincaré sphere.

5.2 Minimum stacking number of anisotropic elements

It is worthwhile to note that, the full coverage of inhomogeneity can also be achieved by using complex in-plane patterns with lower number of layers, which can facilitate our methodology to other wavelength range with profit unit cell configurations and with a trade-off in the bandwidth and angle-sensitivity. Here, we conduct theoretical derivation and full wave simulations to verify the minimum stacking number of anisotropic elements can be decrease to 2.

For a single-layer pattern, the wave matrix (equivalent to Jones matrix, and can be applied to directly multiply for cascading calculation), of any simple shaped component, like rectangular pattern, is $M_{rec} = \begin{bmatrix} m_{xx} & 0 \\ 0 & m_{yy} \end{bmatrix}$, while that of a complex shaped component, such as **L**-shaped element, would be $M_{"L"} = \begin{bmatrix} m_{xx} & m_{xy} \\ m_{xy} & m_{yy} \end{bmatrix}$. For cascading model, the holistic wave matrix of meta-atom with double-layer rectangular patterns is derived as $M_{2-rec} = M_{rec} M_{rec} = \begin{bmatrix} (m_{xx})^2 & 0 \\ 0 & (m_{yy})^2 \end{bmatrix}$, when one of rectangular pattern rotates angle θ, the wave matrix would be:

$$\begin{aligned} M_{2-rec}(\theta) &= M_{rec} R^{-1}(\theta) M_{rec} R(\theta) \\ &= \frac{m_{xx}+m_{yy}}{2}\begin{bmatrix} m_{xx} & 0 \\ 0 & m_{yy} \end{bmatrix} + \frac{m_{xx}\text{-}m_{yy}}{4}\left\{ e^{i2\theta}\begin{bmatrix} m_{xx} & -im_{xx} \\ -im_{yy} & -m_{yy} \end{bmatrix} + e^{-i2\theta}\begin{bmatrix} m_{xx} & im_{xx} \\ im_{yy} & -m_{yy} \end{bmatrix}\right\} \end{aligned} \tag{S26}$$

Different components in two off-diagonal terms in $M_{2\text{-}rec}(\theta)$ are $m_{xx}\sin(2\theta)$ and $m_{yy}\sin(2\theta)$, respectively. It indicates that the degree of inhomogeneity for double-layer rectangular meta-atom only depends on the deviations between m_{xx} and m_{yy}. Meanwhile, for meta-atom with double-layered **L**-patterns, the whole wave matrix is $M_{2-"L"} = M_{"L"} M_{"L"} = \begin{bmatrix} (m_{xx})^2 + (m_{xy})^2 & m_{xx}m_{xy} + m_{xy}m_{yy} \\ m_{xx}m_{xy} + m_{xy}m_{yy} & (m_{xy})^2 + (m_{yy})^2 \end{bmatrix}$, and the matrix changes when rotating one of **L**-element:

$$
\begin{aligned}
M_{2\text{-}``L"}(\theta) &= M_{rec} R^{-1}(\theta) M_{``L"} R(\theta) \\
&= \begin{bmatrix} m_{xx} & m_{xy} \\ m_{xy} & m_{yy} \end{bmatrix} \cdot \left\{ \frac{m_{xx}+m_{yy}}{2} \boldsymbol{I} + \frac{m_{xx}\text{-}m_{yy}+2im_{xy}}{2} e^{i2\theta} \begin{bmatrix} 1 & -i \\ -i & -1 \end{bmatrix} + \frac{m_{xx}\text{-}m_{yy}-2im_{xy}}{2} e^{-i2\theta} \begin{bmatrix} 1 & i \\ i & -1 \end{bmatrix} \right\} \\
&= \frac{m_{xx}+m_{yy}}{2} \begin{bmatrix} m_{xx} & m_{xy} \\ m_{xy} & m_{yy} \end{bmatrix} \\
&\quad + \frac{m_{xx}\text{-}m_{yy}+2im_{xy}}{2} e^{i2\theta} \begin{bmatrix} m_{xx}-im_{xy} & -i\left(m_{xx}-im_{xy}\right) \\ m_{xy}-im_{yy} & -i\left(m_{xy}-im_{yy}\right) \end{bmatrix} + \frac{m_{xx}\text{-}m_{yy}-2im_{xy}}{2} e^{-i2\theta} \begin{bmatrix} m_{xx}+im_{xy} & i\left(m_{xx}+im_{xy}\right) \\ m_{xy}+im_{yy} & i\left(m_{xy}+im_{yy}\right) \end{bmatrix}
\end{aligned} \tag{S27}
$$

The different components in two off-diagonal terms in $M_{2\text{-}``L"}(\theta)$ are functions of (m_{xx}, m_{xy}, m_{yy}), which contains more degrees to modulate the overall inhomogeneity of our meta-atom. This indicates that a minimum of two layers is in principle sufficient if considering cascading complex structures.

To verify the above theoretical assumption for minimum stacking layers of anisotropic elements, we first design meta-atoms with stacking i (i= 1, 2, 3, 4) layers of L-shaped elements, respectively, as shown in Fig. S8B. When only one L-shaped pattern is designed, the degree of inhomogeneity is zero and the corresponding eigen-states are orthogonal no matter the rotation angle. Starting with two layers stacking, the degree of inhomogeneity can already approach 1. When the rotation angle of bottom L-shape element is 90° or 270°, the degree of inhomogeneity reduces due to the increased degree of symmetry for the two-layer L-shaped structures. By increasing the stacking layers to 3 and 4, the unity inhomogeneity degree can be also achieved. Meanwhile, we see that no matter the number of layers of L-shaped elements, one of the two eigen-vector is always distributed along the equator of the Poincaré sphere, while extends away from the equator as a function of the number of layers. This simulation results prove that the minimum stacking layers for anisotropic pattern is two.

On this basis, we conduct full wave simulations of a two-layered **L**-shaped meta-atom, and calculate the frequency and bandwidth responses, eigen-states and eigen-values, and polarization transformation abilities. Fig. S9A presents the schematic of meta-atom, where θ is twisted angle of upper layer **L**-patch and geometric parameters are set as l_1 = 4 mm, l_2 = 8.5 mm, w_1 = w_2 = 1.5 mm. Fig. S9B displays frequency responses within bandwidth 5 GHz – 15GHz of meta-atom with twisted angle θ = 0°, 30°, 60°. When with no twisting effect (θ = 0°), two non-zero off-diagonal elements change in same tendency. The out-of-plane symmetricity is broken with non-zero θ, leading to the decoupling between two off-diagonal elements. This is the necessary condition for non-orthogonal eigen-states as for such less-layer meta-atom configuration. Originated from characteristics of geometric structure, resonance appears and occupies a narrow band around 10 GHz. Then the inhomogeneity performances of this meta-atom model are verified. Fig. S9C shows inhomogeneity parameter of meta-atoms against geometric sizes L_1 and L_2 with twisted angles $\theta = 0°$, 30°, 60°. For meta-atom with no broken symmetricity ($\theta = 0°$), inhomogeneity parameter is around 0. With θ increasing to 30°, degree of inhomogeneity approaches 0.6 and further reach 1 when $\theta = 60°$. Fig. S9D displays the evolution trajectories of eigen-state pairs with θ changing 360°, where eigen polarizations are distributed with no orthogonal restriction. Meanwhile, amplitudes of two eigen-values are also varied with θ, as shown in Fig. S9E. Such results can effectively prove that meta-atom configuration with complex in-plane pattern and less stacking number can also cover full coverage of inhomogeneity and support non-orthogonal eigen formalism. Nevertheless, limited by layer number and complex pattern, bandwidth property is not as wide as for our proposed meta-atom in the main text. Meanwhile, angle-dependence of this **L**-shaped meta-atom is analyzed and shown in Fig. S9F. With incident angle changing from -80° to 80°, degree of inhomogeneity is seriously affected and varies from 0.15 to 0.71, while eigen-states distributions on Poincaré sphere are also transformed dramatically (as shown in the inset). It is seen that although meta-atom with decreased layer number of complex patterns can support our proposed non-orthogonal eigen-formalism, correlated bandwidth and angle dependence performances are accordingly degraded.

Additionally, arbitrary polarization conversion ability of this meta-atom has also been checked. Here we still adopt representative meta-atom (with geometric sizes $l_1 = 4$ mm, $l_2 = 8.5$ mm, $w_1 = w_2 = 1.5$ mm, $\theta = 60°$) as an example and the input state is set as elliptical polarization ($\alpha_{in} = 0.125\pi$, $\beta_{in} = 0$). The polarization conversion efficiency within bandwidth of 8 GHz – 12 GHz (solid blue line) is illustrated in Fig. S9G, and corresponding trajectories of output polarizations vary drastically on the Poincaré sphere in the inset of Fig. S9G. When we fix the output polarization state ($\alpha_{out} = 0.35\pi$, $\beta_{out} = -0.037\pi$, as represented by pink point on Poincaré sphere), output polarization conversion efficiency is displayed by red dotted line in Fig. S9G. At center frequency 10 GHz, the transmittance can approach unity. When shifting to other frequencies, the efficiency seriously decreases, further indicating narrow band property of this meta-atom.

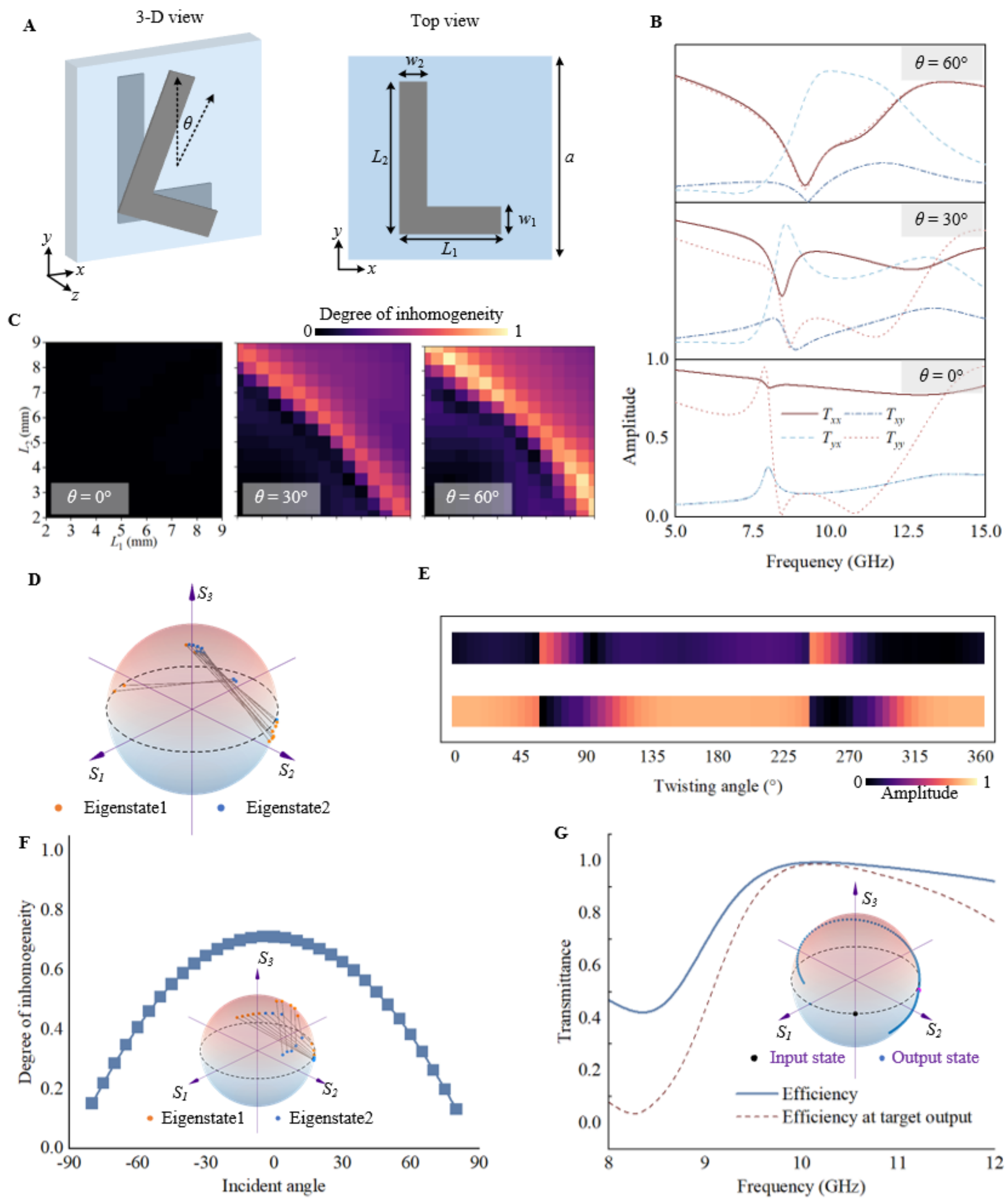

Fig. S9 (A) Schematic of double-layered **L**-shaped meta-atom, θ presents the twisted angle between two **L**-shaped patches. (B) Simulated amplitude profiles of Jones matrix coefficients of meta-atom with different twisted angles $\theta = 0°, 30°, 60°$. (C) Degree of inhomogeneity of meta-atom with different θ against variable geometric sizes L_1 and L_2. (D) Eigen-state pairs and (E) corresponding amplitude responses of eigen-values of meta-atom with θ changing from 0° to 30°. (F) Degree of inhomogeneity of meta-atom under oblique incidence, inset shows corresponding eigen-state pairs. (G) Polarization conversion efficiencies of a representative meta-atom within the operating bandwidth under specific input state, the inset presents input and output state(s) labelled on Poincaré sphere.

Note 6. Supplement demonstrations for eigen-modes of non-orthogonal meta-atoms

6.1 Characterization of dual eigen-states with variable rotation

In main text, we have shown the evolution trends of eigen-state pairs of meta-atoms with different rotation configurations in Jones vector formalism (α_i and β_i). Here, for a clear illustration, we rotate each single patch from 0° to 180° while keeping other two patches fixed, and label the eigen-states evolution trajectories on Poincaré sphere in Figs. S10A - 10C, respectively (the inset shows corresponding rotation scheme). Obviously, the evolution paths of eigen-states $\left|\zeta_{1,2}\right\rangle$ of each rotation situations are not symmetry about the sphere center, sufficiently proving the non-orthogonality of two eigen-states supported by our meta-atoms. When rotating the 1st layered patch with θ_1, eigen-state 1 is confined in the vicinity of x-linear polarization while eigen-state 2 travels a drastic path twice surrounding S_3-axis (Fig. S10A). Such difference between the two evolution paths is due to the asymmetric geometry construction along the normal direction (z-axis) of the meta-atom. When switching to the 2nd layered patch, the trajectories of two eigen-states are symmetry about S_3 (Fig. S10B), which is related to the maintained z-inversion symmetry construction of meta-atom. The situation of rotating 3rd layered patch (Fig. S10C) is a counterpart of that of 1st patch rotation, highlighting the reciprocity of the proposed passive stacked meta-atom.

Additionally, we present the precise characterization of non-orthogonal eigen-states of proposed meta-atom with variable θ_1, θ_2 and θ_3, where the corresponding Jones vector angles $\alpha_{1,2}$ and $\beta_{1,2}$ are exhibited in Figs. S10D and 10E. Among the six α profiles of two eigen-states, the coverage of α_1 with variable θ_1 is limited to 5°, while the corresponding α_2 covers the range from 19° to 90°, indicating that the corresponding eigen-state 1 insensitively approaches x-linear polarization state when changing θ_1. The similar situation happens to meta-atom with variable θ_3, whose eigen-state 2 is close to y-linear polarization state. Besides, the $\alpha_{1,2}$ tendency of meta-atom with rotated θ_2 are mirrored symmetric with respect to 45°, which determines the symmetrical center of evolution paths of two eigen-states on Poincaré sphere is $S_1 = 0$ plane. As for β profiles representing for phase difference between two linearly polarized components in eigenvectors, the phase responses of twisting configuration with independent variate θ_1, θ_2, θ_3 all can fully cover -180° to 180°, implying that there is no phase restriction of proposed non-orthogonal meta-atom on birefringence. Notably, 180°-interruptions appearing in all β-profiles, when the rotation angles are equal to 90°, are originated from the change of phase difference sign between x- and y-polarized components in corresponding Jones vectors, and 90°-interruptions shown in β-profiles when θ_2 = 55° and 127° are induced by the elliptical eigen-state conversion from [S_1, S_2, S_3] to [S_1, -S_2, S_3].

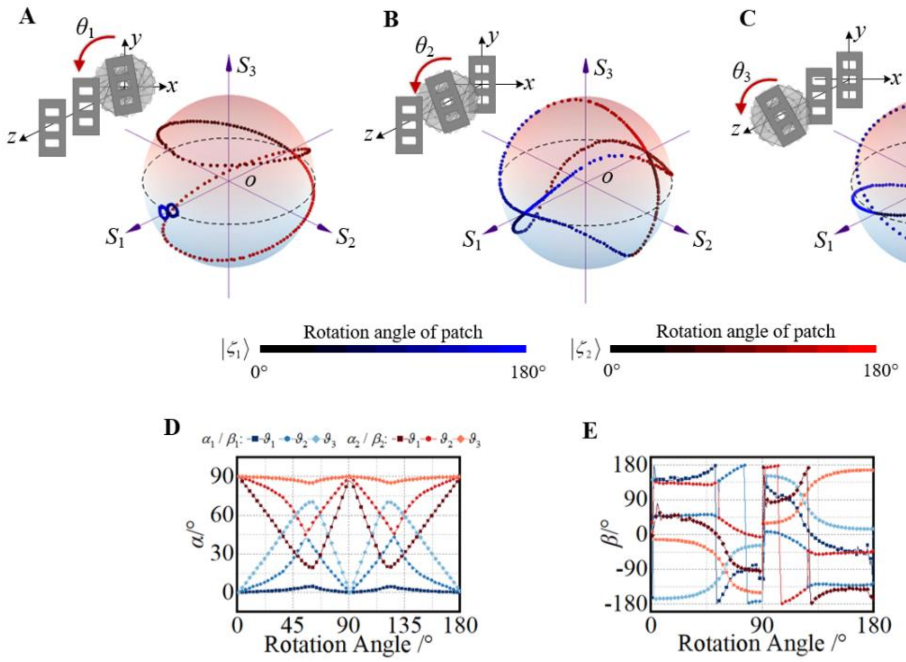

Fig. S10 Evolution trajectories on the Poincaré sphere of eigen-state pairs of meta-atom with variable orientation of (A) 1st layered patch with θ_1, (B) 2nd layered patch with θ_2, (C) 3rd layered patch with θ_3. Characterization of eigen polarization pairs with variable rotated patch layers in Jones vector formulism of (D) α_i ($=\arctan\left(|\zeta_{iy}|/|\zeta_{ix}|\right), \in[0,\pi/2]$) and (E) β_i ($=\angle\zeta_{iy}-\angle\zeta_{ix}, \in[-\pi,\pi]$).

6.2 Corresponding eigen-values representation

Based on Eq. (S3), we can calculate the eigen-values according to the simulated scattering parameters. Fig. S11 exhibits the calculated eigen-values of the meta-atom with rotation of separate patch layers of θ_1, θ_2, θ_3. Eigen-value 1, labelled as blue dots, is confined around the original point in complex field, which corresponds to the tilted double-circle shaped trajectory of eigen-state1 on Poincaré sphere. Meanwhile the dotted eigen-value 2 is more dispersive with the first patch layer rotated from 0° to 180°. When θ_1 is individually varying, the real and imaginary parts of eigen-values of meta-atom are shown in Fig. S11A, where two components exhibit distinct tendencies. Fig. S11B shows the eigen-values of meta-atom that is constructed with only middle patch rotated. We can observe that two eigen-values exhibit different tendencies and interruptedly exchanged at θ_2 = 55° and 127°, which corresponds to the phase interruption at the exact point of θ_2 as explained in the previous part. The eigen-values of meta-atom with varying θ_3 are shown in Fig. S11C, where the distributions of eigen-values show same tendency as for meta-atom with variable θ_1, attributing to the reciprocity of the proposed non-orthogonal meta-atom configuration.

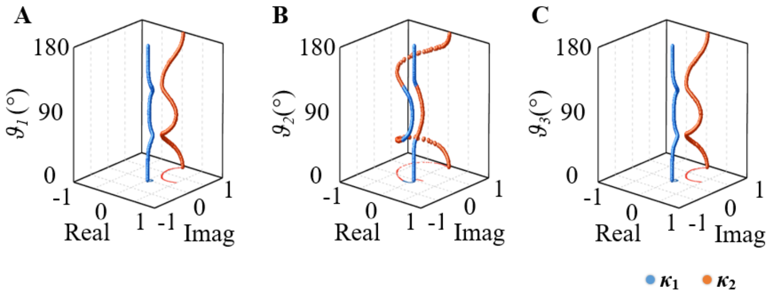

Fig. S11 Corresponding eigen-values of non-orthogonal meta-atom with rotating different patches (A) 1st layered patch with θ_1, (B) 2nd layered patch with θ_2, (C) 3rd layered patch with θ_3.

Note 7. Fabrication and measurement methods in microwave region.

7.1 Microwave fabrication of multilayered metasurface samples.

The prototypes proposed in this paper are fabricated by classic printed circuit board (PCB) technique. In the fabrication process, meta-structures are implemented with four pieces of polyfluortetraethylene dielectric-slabs and three adhesive layers. The 1 mm-thick dielectric substrates have a relative permittivity $\varepsilon_r = 3.5$ and double copper-cladding layer of 0.035 mm-thick, while the adhesive layer has a relative permittivity $\varepsilon_r = 2.74$ and thickness of $t_{ad} = 0.1$ mm. The total thickness of fabricated samples is 4.475 mm (about $0.15\lambda_0$ at 10 GHz). The non-orthogonal metasurface samples for verifying polarization transformation are fabricated with 15 × 15 meta-atoms, and the photographs of all 13 fabricated samples are shown in Fig. S12. Meanwhile, metasurfaces for gating CP channels consist of 31 × 31 meta-atoms, and the fabrication tolerance is in accordance with initial design requirements, whose photograph is reprehensively shown in Fig. 4B in main text.

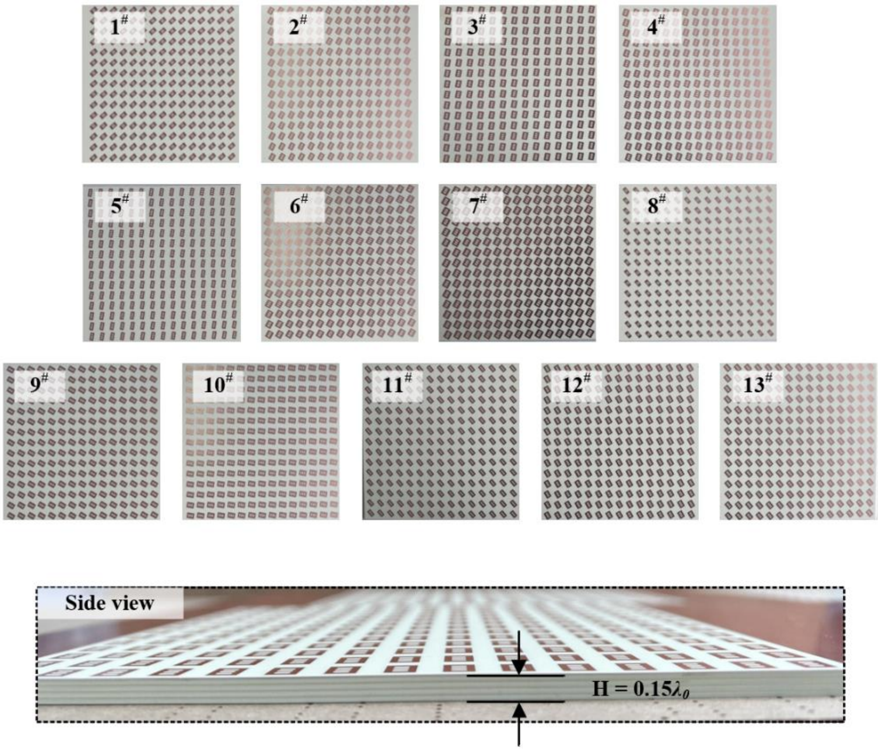

Fig. S12 Photographs of 13 fabricated non-orthogonal metasurface samples for arbitrary polarization transformation demonstration.

7.2 Error analyses of adhesive layer thickness in fabrication process

In order to analyze the fabrication error effect of such adhesive layers, we conduct simulations on meta-atoms with different thickness of adhesive layers. Fig. S13A displays schematic of fabricated multi-layered metasurface, and Figs. S13B and S13C display the frequency profiles against variable thickness

t_{ad}. Here we adopt a meta-atom with no twisting configuration, which facilitates eigen-state pairs as *x*- and *y*-linear polarizations, respectively. In this case, two eigen-values are two diagonal elements in Jones matrix, i.e., t_{xx} and t_{yy}, while two off-diagonal elements are both zero. The amplitude tendencies of two eigen-values can be maintained even after modification of the adhesive layer thickness. It is noted that when the adhesive layers get thicker, the insertion loss in the band-pass profiles of $|t_{xx}|$ and $|t_{yy}|$ can be optimized, while the bandwidth are slightly reduced. Nevertheless, the variations are quite small to affect performances of proposed meta-atom.

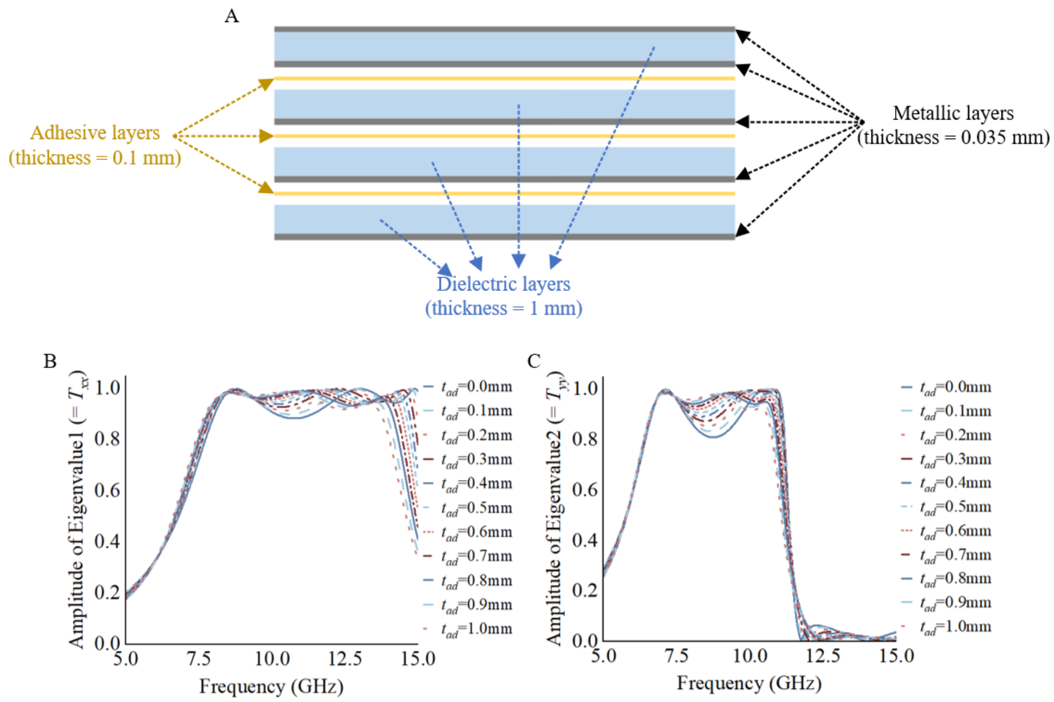

Fig. S13 (A) Schematic of fabricated multi-layered meta-atom configuration. Simulated amplitude responses of (B) eigen-value1 and (C) eigen-value2 of meta-atom with variable thickness from 0.0 mm to 1.0 mm with interval 0.1 mm of meta-atom within bandwidth 5 GHz – 15 GHz.

7.3 Experimental measurements.

For arbitrary polarization transformations: The scattering parameter measurements in microwave region are conducted by a setup surrounded by microwave absorbers in anechoic chamber to minimize parasitic reflections, as shown in Fig. S14A. The Agilent 8722ES vector network analyzer (VNA) is used to collect the complex scattering field information, including both amplitude and phase responses of the field component. Two 2 GHz - 18 GHz dual-polarized wideband horn antennas are used as the transmitting and receiving ends. The distance between the transmitting antenna and the samples is more than $20\lambda_0$, so that the incident wavefront approaches the quasi-plane incident wave. The distance between the sample and the receiving antenna exceeds $100\lambda_0$ (calculated by $2D^2/\lambda_0$, where D = 210 mm is the diagonal size of sample) to achieve far-field scattering condition. As mentioned in main text and Note 2, the output polarization state $\left|\vec{\boldsymbol{E}}^{out}\right\rangle = \boldsymbol{J}\left|\vec{\boldsymbol{E}}^{in}\right\rangle$ and the corresponding conversion efficiency $T = \frac{\left\langle \vec{\boldsymbol{E}}^{out} \middle| \vec{\boldsymbol{E}}^{out} \right\rangle}{\left\langle \vec{\boldsymbol{E}}^{in} \middle| \vec{\boldsymbol{E}}^{in} \right\rangle} = \frac{\left\langle \vec{\boldsymbol{E}}^{in} \middle| \boldsymbol{J}^{\dagger}\boldsymbol{J} \middle| \vec{\boldsymbol{E}}^{in} \right\rangle}{\left\langle \vec{\boldsymbol{E}}^{in} \middle| \vec{\boldsymbol{E}}^{in} \right\rangle}$, both can be obtained by operation of transmission matrix $\boldsymbol{J}$ and preset input state $\left|\vec{\boldsymbol{E}}^{in}\right\rangle$. Thus, it is important to obtain the measured scattering matrix $\boldsymbol{J}$ with quadruplex complex coefficients in linear polarization base. The four transmission coefficients, J_{xx}, J_{xy}, J_{yx}, J_{yy} in the matrix $\boldsymbol{J}$, are obtained by setting both the source and the receiver dual-polarized horn antennas, and therefore the polarization axis, along horizontal and vertical direction to produce and receive x- and y-linearly polarized electric fields, respectively. Consequently, the quadplex transmission field-components in linear polarization base can be one-by-one measured. Thereafter, the output polarization states, and measured efficiencies of the input-output polarization conversion are confirmed with the pre-determined input state, and the additional eigen-values, eigen-states, and inhomogeneity degrees can be fully calculated from the matrix $\boldsymbol{J}$. The transmission coefficient under the same setup without interposing along the beam path any metasurface is used as the normalization standard.

For near-field detection: Near-field detection is also conducted by a setup surrounded by microwave absorbers in anechoic chamber. The schematic is illustrated in Fig. S14B. The Agilent 8722ES (V.N.A.) is also used to record the complex transmission field information (S_{21} parameters), including both amplitude and phase responses of each polarization component. A 2 GHz - 18 GHz dual circularly polarized wideband horn antenna is used as the feeding source to launch the quasi-plane waves by enlarging the distance relative to metasurface more than $20\lambda_0$. For the near-field mapping detection, a fiber optic active antenna is used as a field probe to measure both the amplitude and phase of the electric field. This fiber probe has an ultrasmall purely dielectric head of 6.6 × 6.6 mm^2, owning portability and movable abilities, and negligible field perturbation (details in *http://www.enprobe.de/datasheets/EFS-105.pdf*). The probe receiver is fixed on two translation stages controlled by a motion controller and its position is incremented by a step of 2 mm. Thus, the probe receiver engineered by motion controller can be used to collect the output electric field information covering the whole detection xy plane with specific propagation z distance. Herein, the range of detection region is the same as the preset imaging size, i.e. about $10\lambda_0 \times 10\lambda_0$, with focal distance $z = 5\lambda_0$. Notably, the receiver fiber probe can only be conducted along horizontal and vertical directions to collect x- and y-linearly polarized fields, i.e., E_x and E_y components. Transmission electric fields for left- and right-handed circular polarizations is obtained simply using the expressions $E_L = E_x + iE_y$ and $E_R = E_x - iE_y$, respectively. Through combining different polarizations of source antenna, the quadruplex transmission field components in the circular polarization base can be measured, including L-output under L-input, termed as complex component T_{LL}, the R-output under L-input as T_{RL}, the L-output under R-input as T_{LR}, and the R-output under R-input as T_{RR}. Then, the complex electric distribution in the whole imaging region can be obtained, including quadruplex circularly polarized transmission channels. The required CP gating effects and the holographic profiles can be calculated through energy intensities and phase distributions. The setups for these two measurements are comparably listed in Table. S2.

Table S2. Setups comparison between two adopted measurements

		Arbitrary polarization conversion	**Near-field hologram imaging**
Source end	Transmitting device	horn antenna	
	Polarization mode	Dual linear polarizations x- & y-	Dual circular polarizations LHCP & RHCP
	Illumination method	Normal & oblique	Normal
	Distance to sample	$> 20\lambda_0$	
Analyzer		Agilent 8722ES vector network analyzer (VNA)	
Receiver end	Receiving device	Dual linearly polarized horn antenna	Dual linearly polarized fiber probe
	Polarization mode	Dual linear polarizations x- & y-	Dual linear polarizations x- & y-
	location	Local point Aligning to sample center	Global imaging region Scanning range $10\lambda_0 \times 10\lambda_0$
	Distance to sample	$> 100\lambda_0$	$= 5\lambda_0$
Schematic		Fig. S14A	Fig. S14B

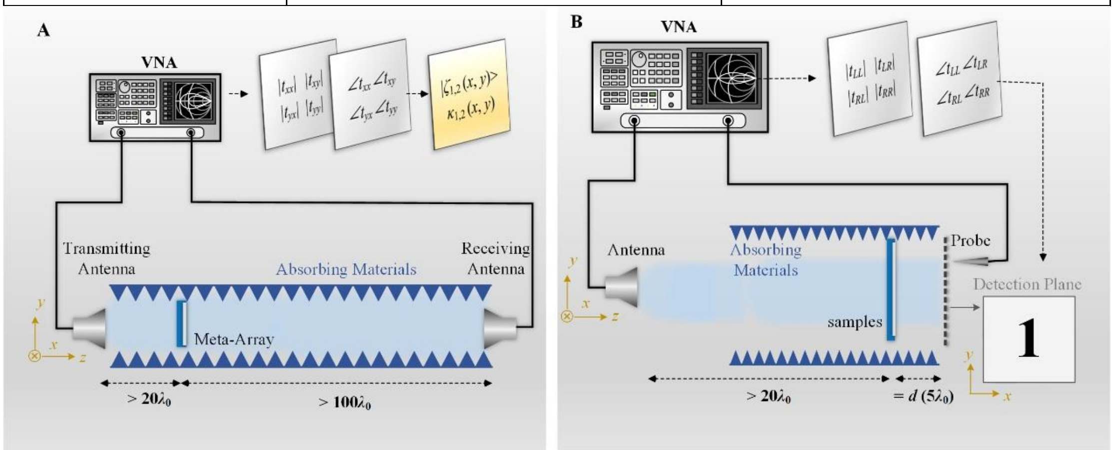

Fig. S14 Schematic of experimental setups for (A) arbitrary polarization transformation measurement and (B) near-field detection measurement.

Note 8. Bandwidth performance and additional demonstrations for high-efficient arbitrary polarization transformations

8.1 Bandwidth performances of proposed non-orthogonal metasurfaces in measurements.

To explore the bandwidth performances for arbitrary polarization conversions, we consider transmittance property and polarization conversion efficiency for bandwidth evaluations by three representative samples (11#, 12#, 13#). Firstly, the transmittance within operating bandwidth (8 GHz – 12 GHz, relative bandwidth of 40%) are calculated according to Eq. (2) by considering frequency *f*: $T_{MS}(f)=\frac{\langle \vec{\boldsymbol{E}}^{out}(f)|\vec{\boldsymbol{E}}^{out}(f)\rangle}{\langle \vec{\boldsymbol{E}}^{in}|\vec{\boldsymbol{E}}^{in}\rangle}$, which are represented in Fig. S15 (Fig. 3E in main text). It is worth noting that our meta-atom is composed of multiple metallic and dielectric layers, owning unavoidable frequency dispersions, which would result in the polarization variations within the operating bandwidth. This means the output polarizations would be variable against to *f*, and the output states at different frequencies of three samples on Poincaré spheres are displayed in the insets of Fig. S15, respectively. When considering frequency dispersion, the output polarization states would move in certain trajectories, almost spanning half of polarization space, carrying the diversity of the polarization information.

Then, we evaluate the directed polarization conversion efficiencies of these three samples, including 11# for transforming *x*-linearly polarized state (α = 0, β = 0) to A state (α = 0.19π, β = 0.61π), 12# for *x*-linearly polarized state to B state (α = 0.22π, β = 0.55π), 13# for *x*-linearly polarized state to C circular state (α = 0.25π, β = 0.5π), which are labelled by black dots in the insets of Fig. S16. This customized polarization conversion efficiency is calculated by $T_{MS}=\frac{\langle \vec{\boldsymbol{E}}^{target}|\vec{\boldsymbol{E}}^{target}\rangle}{\langle \vec{\boldsymbol{E}}^{in}|\vec{\boldsymbol{E}}^{in}\rangle}$, where $|\vec{\boldsymbol{E}}^{target}\rangle=|\langle \vec{\boldsymbol{E}}^{out}|\vec{\boldsymbol{E}}^{target}\rangle||\vec{\boldsymbol{E}}^{out}\rangle$ represents the intensity of target output state in projection of transformed state. Measured polarization conversion efficiencies of three samples are illustrated in Fig. S16, where peak values appear at the working frequency 10 GHz, indicating that directed input output polarization conversion can be optimally achieved. With frequency shifting, the efficiencies are accordingly degraded due to the polarization dispersion performances. Even so, the bandwidth performances can still prove the achievability and feasibility of our proposed non-orthogonal metasurface for arbitrary polarization conversions with extremely high efficiencies.

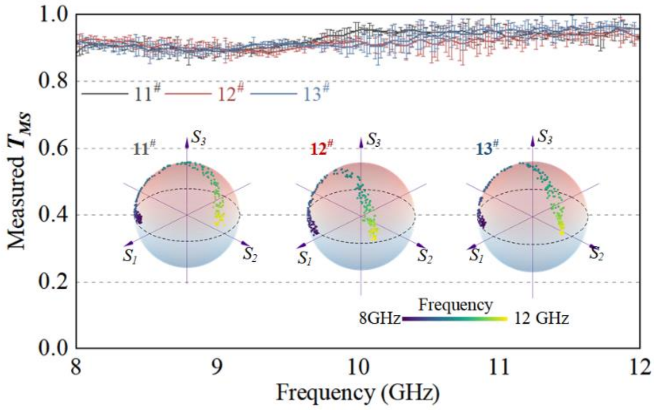

Fig. S15 Measured bandwidth properties of samples (11#, 12#, 13#), where error bars show the corresponding noisy fluctuations in the measurement processes, and insets present output polarization states under specific input state within 8 GHz – 12 GHz, respectively.

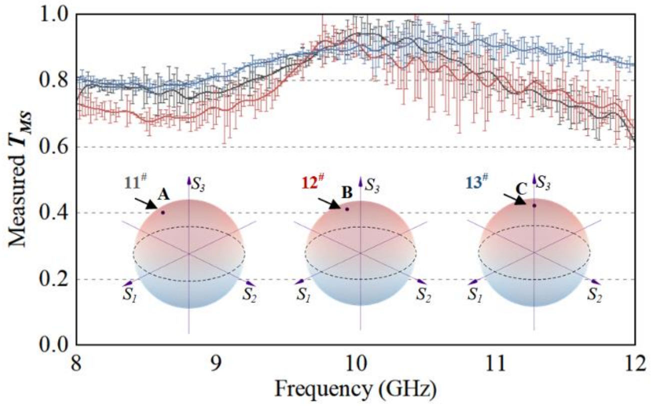

Fig. S16 Measured polarization conversion efficiencies of samples (11#, 12#, 13#) within 8 GHz – 12 GHz, respectively, error bars show the corresponding noisy fluctuations in the measurement processes, and insets present the target output polarization state that transformed from a specific input state.

8.2. Fixed input state – variable output states

Here, input state is set as x-linear polarization (Stokes parameters $\left|\vec{E}_A^{in}\right\rangle = \begin{bmatrix}1\\0\\0\end{bmatrix}$), while target output state is set along dash path on Poincaré sphere ($\left|\vec{E}_B^{out}\right\rangle = \begin{bmatrix}\cos(2\chi_{pre})\cos(2\varphi_{pre})\\ \cos(2\chi_{pre})\sin(2\varphi_{pre})\\ \sin(2\chi_{pre})\end{bmatrix} \begin{cases}2\varphi_{pre} = \pm 45°, \pm 135°\\ 2\chi_{pre} \in [-90°, 90°]\end{cases}$) in Fig. S17A. We uniformly sample 48 representative elliptical polarizations as output states, and then establish corresponding non-orthogonal metasurfaces with optimized geometric twisting angles to achieve required polarization transformation processes. Numerically simulated output polarization states of meta-arrays are marked as discrete dots on Poincaré sphere in Fig. S17A, whose top view is shown in the inset. All the output states are distributed closely around the pre-defined path on Poincaré sphere, indicating that x-linearly polarized input can be successfully transformed into target polarized state by meta-atoms with tailorable non-orthogonal eigen-states. The azimuth and declination angles (2φ and 2χ) of ideally pre-set and simulated results of output states are displayed in Fig. S17B. The RMSE of elliptical azimuthal angle 2φ is 5.4° and that of declination angle 2χ is 4.4°. These slight deviations are caused by the pre-set error tolerances of elliptical angles as ±5° (relative to $2\varphi_{pre}$ and $2\chi_{pre}$). These barely undistorted polarization responses successfully validate the polarization modulation ability by non-orthogonal metasurfaces with designed eigen-states. Fig. S17C displays the simulated efficiencies of proposed meta-arrays for this single polarization input to single output case. The simulated average efficiency reaches 95% with the maximum as 99%.

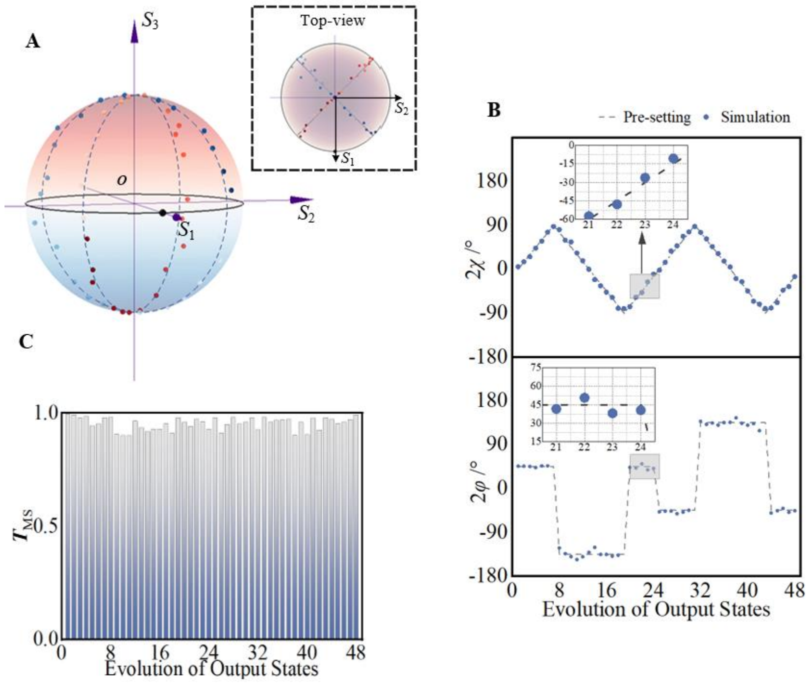

Fig. S17 Supplement demonstrations of polarization transformations from fixed input state to variable output states. (A) Under the x-linearly polarized incidence, the pre-defined (dash line) and simulated (discrete dots) output polarization states evolute along the path on Poincaré sphere, the inset presents the top-view of Poincaré sphere. (B) Calculated and simulated 2φ and 2χ of output states. (C) Simulated efficiency of non-orthogonal samples.

8.3. Variable input states – fixed output state

In this part, we set input state varies along the dotted line on Poincaré sphere as shown in Fig. S18A and the output state to be fixed by RHCP state with Stocks parameters [0, 0, 1]. Similarly, we optionally choose sampled 48 representative input elliptical polarization states along the pre-set trajectory, and the corresponding 2φ and 2χ of ideal input states are displayed by solid and hollow dots in Fig. S18B. To implement such arbitrary polarization transformation processes, we also employ 48 non-orthogonal metasurfaces with profitable eigen-state pairs. Under the illuminations with changeable input polarization states, all simulated output states (blue solid dots on Poincaré sphere) are assembled around the north point from the top-view shown in the inset of Fig. S18A, indicating that pre-defined representative input polarization states are successfully transformed into RHCP as theoretically required. Meanwhile, the elliptical azimuthal and declination angles of transmitted field polarizations are displayed in Fig. S18C, where the deviation between simulated and ideal output polarization response is illustrated by the error bar. Accordingly, the RMSE of elliptical declination angle is 5.4°. It is noted that due to the particularity of the north point RHCP, whose declination angle 2χ is fixed to 90°, there exist fewer restrictions on corresponding azimuthal angles of the input states. Fig. S18D presents the transmission efficiency of 48 meta-arrays, where each output polarization states can be achieved with high transmittance under different polarized incident wave. The average efficiency of 48 meta-arrays can reach 97% in this demonstration, effectively verifying the modulation performances of proposed non-orthogonal eigen polarization mechanism.

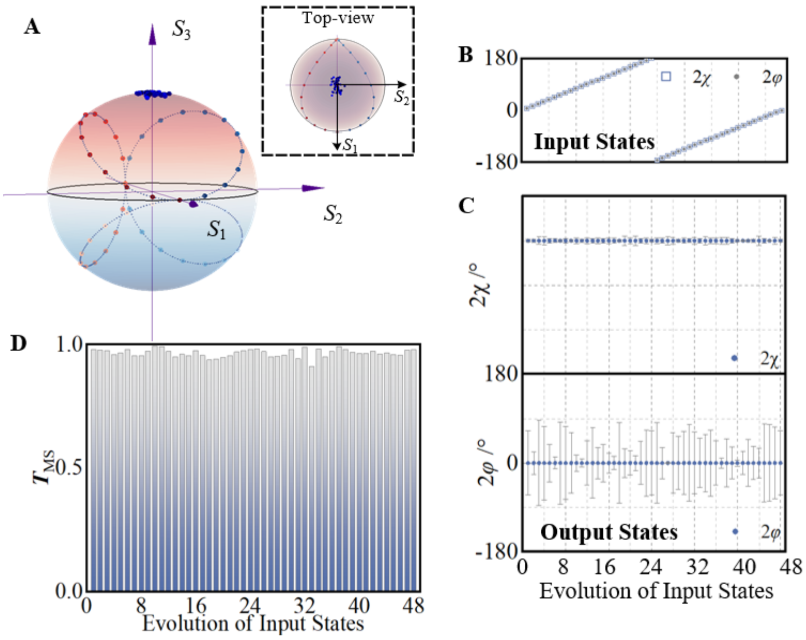

Fig. S18 Supplement demonstrations of polarization transformations with variable input states –fixed output state. (A) Pre-defined input and output polarization states labelled on Poincaré sphere, inset shows the top-view. (B) Theoretical elliptical angles of variable input states. (C) Theoretical and simulated elliptical angles of output polarization states. (D) Simulated efficiency of all 48 verified meta-arrays.

8.4 Demonstrations on conventional linear/circular polarization conversion.

Here, we also supplement several classical polarization conversion cases, including input x - output y, and input circular - output linear polarization transformation.

A) Input x - output y linear polarization transformation

The parameter sizes of proposed meta-atom configuration are set as p_x = 7.5 mm, p_y = 1.6 mm, $\theta_1 = 0°$, $\theta_2 = 30°$, $\theta_3 = 60°$. Based on this meta-atom configuration, polarization transformation from $\boldsymbol{P_{in}}$ state with [α = 0.0 π, β = 0.0 π] to $\boldsymbol{P_{out}}$ state with [α = 0.5 π, β = 0.0 π], as schematically shown in Fig. S19A, can be obtained with efficiency 91.52% at operating frequency 10 GHz, and effective Jones matrix can be expressed as $J_{X-Y} = \begin{bmatrix} -0.0978 + 0.0517i & 0.3406 + 0.1911i \\ -0.7195 - 0.5547i & 0.1668 + 0.2397i \end{bmatrix}$. The bandwidth output efficiency is presented in Fig. S19B.

B) Input circular - output linear polarization transformation

In order to achieve polarization transformation for from $\boldsymbol{P_{in}}$ state with [α = 0.25 π, β = 0.5 π] to $\boldsymbol{P_{out}}$ state with [α = 0.0 π, β = 0.0 π], as schematically shown in Fig. S19C. The proposed meta-atom is designed with p_x = 3.3 mm, p_y = 6.9 mm, $\theta_1 = 0°$, $\theta_2 = 10°$, $\theta_3 = 20°$ and operating Jones matrix is $J_{CP-LP} = \begin{bmatrix} -0.3590 + 0.7047i & 0.4262 + 0.3782i \\ 0.4262 + 0.3782i & -0.0446 - 0.5660i \end{bmatrix}$. The obtained transmission efficiency within bandwidth is displayed in Fig. S19D, and peak efficiency is 95.5% at center frequency 10 GHz.

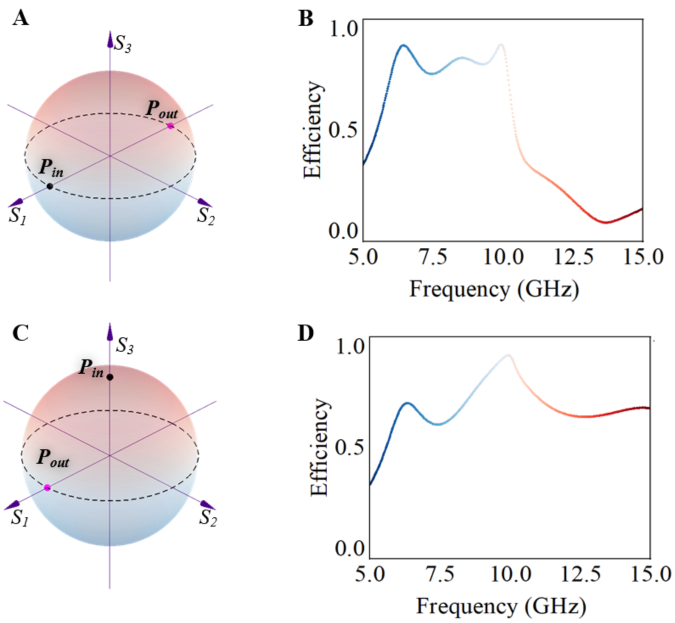

Fig. S19 (A) Schematic of input x - output y linear polarization transformation on Poincaré sphere, and

(B) corresponding efficiency profile of proposed meta-atom within bandwidth. (C) Schematic of input circular - output linear polarization transformation on Poincaré sphere, and (D) corresponding efficiency profile of proposed meta-atom within bandwidth.

Note 9. Applicability demonstrations of non-orthogonal metasurfaces at optical and infrared wavelength regions

In order to further verify that our proposed non-orthogonal eigen formalism can be theoretically adopted with no limitation on wavelength, we design two meta-atom configurations working in distinct optical wavelength regimes.

First, we shift the similar configuration as used in the main text to infrared region of 1550 nm. The unit cell is composed with five layers of aluminum film and four polyimide spacers, as shown in Fig. S20A. A representative meta-atom is selected to present required non-resonant band-pass responses, whose geometric parameters includes, periodic size a = 500 nm, width p_x = 150 nm and length p_y = 350 nm of aluminum film, the radius of grid aperture is r = 190 nm, the thickness of aluminum and polyimide layers are t = 10 nm and h = 50 nm. The key factor for non-orthogonal eigen-state pairs is the variable twisted angles θ_1, θ_2 and θ_3 of different aluminum films. Fig. S20B displays the simulated amplitude profiles of transmission spectra under linear polarizations, exhibiting the pass-band performance of proposed equivalent filter model. The loss in amplitude profiles is attributed to the dispersion characteristics of optical metal material. Meanwhile, when twisted angles θ_1 = 0°, θ_2 = 30° and θ_3 = 60°, the spectrum profiles are illustrated in Fig. S20C, two cross-polarized components get differentiated and non-zero, satisfying necessary condition for non-orthogonal eigen-state pairs. To further verify the non-orthogonality performances at 1550 nm, the evolution trajectories of eigen-state pairs, intensity mappings of inhomogeneity degree are displayed in Figs. S20D and S20E. When twisted angle θ_2 and θ_3 changing from 0° to 360°, the non-orthogonality properties of eigen-state pairs are variable and could effectively cover from 0 to 1. Fig. S20F shows the intensity mappings of eigen-values with variable θ_2 and θ_3, indicating sufficient degree of freedoms for diattenuation and phase retardances modulations.

The other verification is conducted by pure dielectric meta-atom with operating wavelength 600 nm. Meta-atom is designed with double-layered **L**-shaped configuration, as schematically shown in Fig. S21A, whose geometric parameters are labelled by l_1, l_2, w_1, w_2, periodic size is a = 500 nm, and relative twisting angle is θ. Fig. S21B displays simulated amplitude profiles of meta-atom with no rotation in the bandwidth 595 nm - 605 nm. Due to the antistrophic in-plane pattern, the diagonal coefficients are maintained over 0.85 separately and the corresponding off-diagonal coefficients show same non-zero tendency, conforming to the in-plane asymmetric characteristics. When θ increases to 30°, the amplitude profiles in band are presented in Fig. S21C. Accordingly, two off-diagonal tendencies are decoupled against wavelength, and an obvious resonant appears around 600 nm. These in-band performances verify the characteristics of such double-layered resonant meta-atom, and support non-orthogonal eigen-modes. Then we observe the corresponding eigen responses at 600 nm. With twisting angle increasing from 0° to 360°, inhomogeneity parameter changes accordingly, as shown in Fig. S21D, revealing the full coverage from 0 to 1. Here we set the input as an arbitrary elliptical polarization (α = 0.25π, β = 0.25π), the trajectories of output polarizations vary drastically on the Poincaré sphere (Fig. S21E), and efficiency of polarization transformation would be degraded when shifting away from operating wavelength (Fig. S21F).

From these results we can conclude that the proposed non-orthogonal eigen-formalism for high efficiency arbitrary polarization conversions can be successfully expanded and applied to optical regime by adopting profit meta-atom configurations. It is worth noting that, under the full coverage of inhomogeneity requirements, the functional layer number of meta-atom can be reduced by increasing complexity of in-plane patterns, which would be a potential capacity for wavelength expansion. Although this double-layered dielectric meta-atom can only work in a narrow bandwidth and is sensitive to the incident angle, the corresponding non-orthogonal eigen-modes and arbitrary elliptical polarization conversion ability are completely supported.

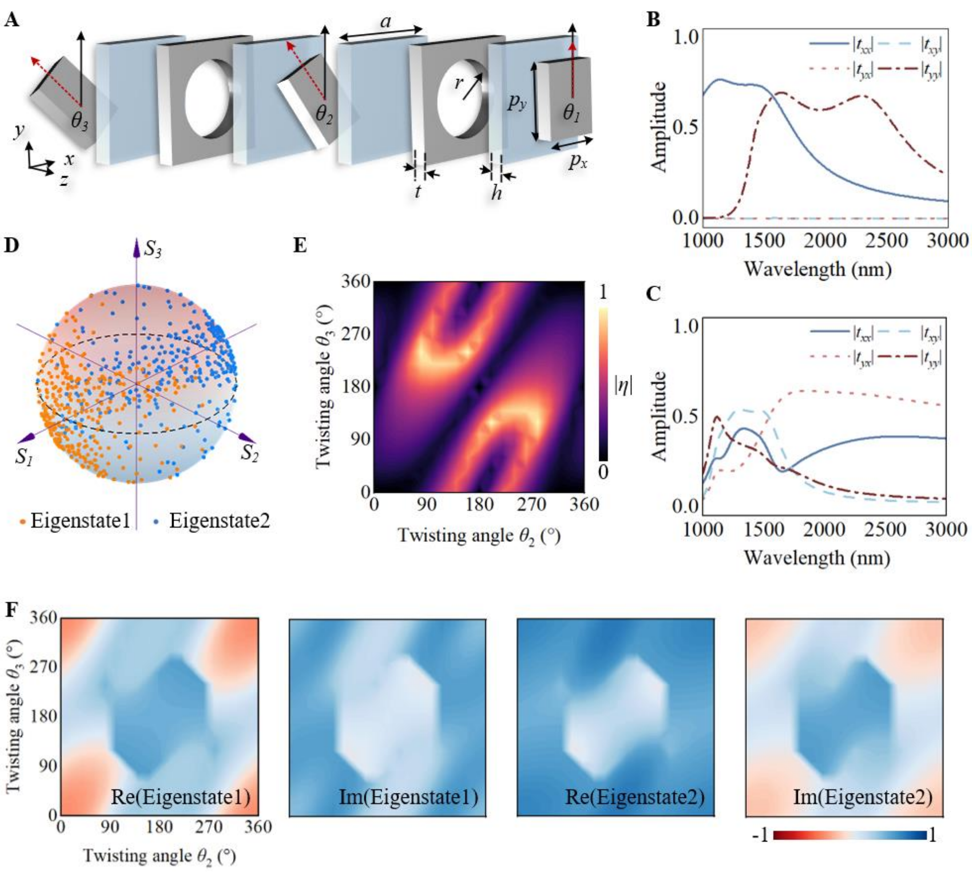

Fig. S20 (A) Schematic of multilayered meta-atom expanded to 1550 nm. Simulated amplitude responses of coefficients in Jones matrix within bandwidth of meta-atoms with twisting angles (B) $\theta_1 = \theta_2 = \theta_3 = 0°$ and (C) $\theta_1 = 0°$, $\theta_2 = 30°$, $\theta_3 = 60°$. (D) Eigen-state pairs and (E) degree of inhomogeneities of meta-atom with twisting angle θ_2 and θ_3 changing from 0° to 180° ($\theta_1 = 0°$). (F) Intensity mappings of real and imaginary parts of eigen-values of meta-atom with variable θ_2 and θ_3.

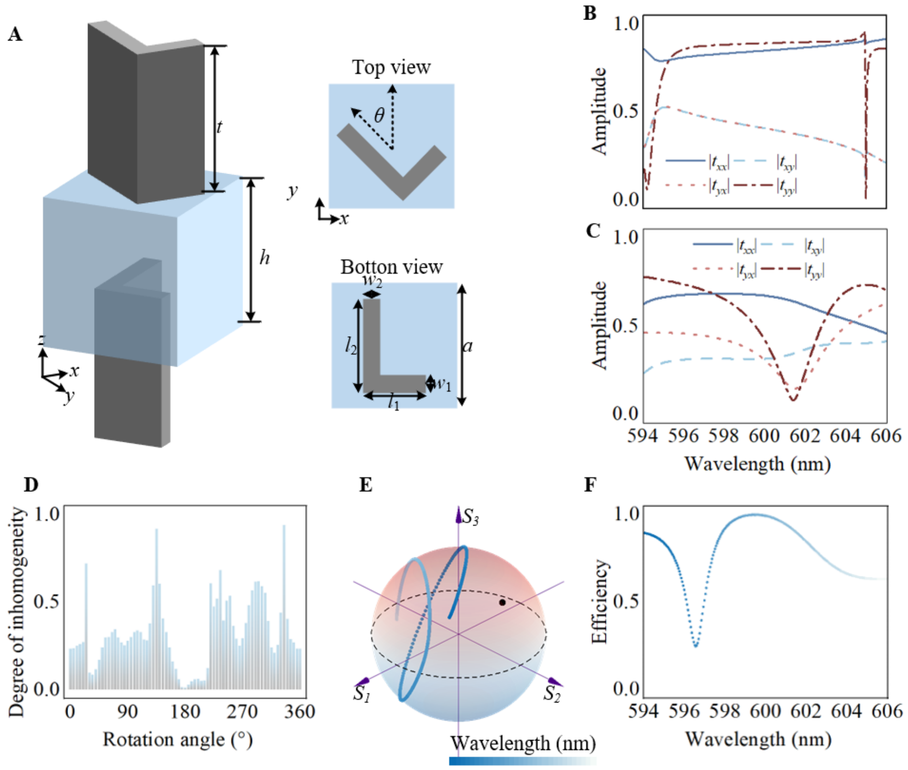

Fig. S21 (A) Schematic of proposed double-layered **L**-shaped meta-atom working at 600 nm, θ presents the twisting angle between two **L**-shaped patches as the key factor for non-orthogonal eigen-mode. Simulated amplitude profiles of Jones matrix coefficients with different twisting angles (B) $\theta = 0°$ and (C) 30°, respectively. (D) Degree of inhomogeneity with different θ changing from 0° to 360°. (E) The preset input state and the corresponding trajectory of output states within bandwidth of a representative meta-atoms labelled on Poincaré sphere. (F) Polarization conversion efficiencies of representative meta-atom within the operating bandwidth under specific input state.

Note 10. Supplement analyses and results of full C_4^i gating of CP channels

10.1 Plural coefficients $m_{1,2}$ and $n_{1,2}$ verification.

As introduced in the main text, any pair of eigen-states $|\zeta_{1,2}\rangle$ can be decomposed into LHCP state $|L\rangle$ and RHCP state $|R\rangle$ with two distinct plural coefficients $\boldsymbol{m}_{1,2}$ and $\boldsymbol{n}_{1,2}$, respectively ($|\zeta_{1,2}\rangle = \boldsymbol{m}_{1,2}|L\rangle + \boldsymbol{n}_{1,2}|R\rangle$ and $\boldsymbol{\eta} = \boldsymbol{m}_1^*\boldsymbol{m}_2 + \boldsymbol{n}_1^*\boldsymbol{n}_2$). According to the inherent steadiness associated to eigen polarization states passing through analogue-chiral element $\boldsymbol{J}$, the transmission process $\boldsymbol{J}|\zeta_{1,2}\rangle = \boldsymbol{\kappa}_{1,2}|\zeta_{1,2}\rangle$ can be depicted as:

$$\boldsymbol{J}|L\rangle = F_{LL}\left(\boldsymbol{\kappa}_{1,2}, |\zeta_{1,2}\rangle\right)|L\rangle + F_{RL}\left(\boldsymbol{\kappa}_{1,2}, |\zeta_{1,2}\rangle\right)|R\rangle = \frac{\boldsymbol{\kappa}_1\boldsymbol{m}_1\boldsymbol{n}_2 - \boldsymbol{\kappa}_2\boldsymbol{m}_2\boldsymbol{n}_1}{\boldsymbol{m}_1\boldsymbol{n}_2 - \boldsymbol{m}_2\boldsymbol{n}_1}|L\rangle + \frac{\boldsymbol{n}_1\boldsymbol{n}_2\left(\boldsymbol{\kappa}_1 - \boldsymbol{\kappa}_2\right)}{\boldsymbol{m}_1\boldsymbol{n}_2 - \boldsymbol{m}_2\boldsymbol{n}_1}|R\rangle \tag{S28a}$$

$$\boldsymbol{J}|R\rangle = F_{LR}\left(\boldsymbol{\kappa}_{1,2}, |\zeta_{1,2}\rangle\right)|L\rangle + F_{RR}\left(\boldsymbol{\kappa}_{1,2}, |\zeta_{1,2}\rangle\right)|R\rangle = \frac{\boldsymbol{m}_1\boldsymbol{m}_2\left(\boldsymbol{\kappa}_2 - \boldsymbol{\kappa}_1\right)}{\boldsymbol{m}_1\boldsymbol{n}_2 - \boldsymbol{m}_2\boldsymbol{n}_1}|L\rangle + \frac{\boldsymbol{\kappa}_2\boldsymbol{m}_1\boldsymbol{n}_2 - \boldsymbol{\kappa}_1\boldsymbol{m}_2\boldsymbol{n}_1}{\boldsymbol{m}_1\boldsymbol{n}_2 - \boldsymbol{m}_2\boldsymbol{n}_1}|R\rangle \tag{S28b}$$

Where $\boldsymbol{F}_{uv}$ (the subscript u and v represents output and input state as LHCP or RHCP) denotes CP transmission coefficient. Therefore, we can deliberately select i (i = 1, 2, 3, 4) and suppress the other (4 - i) channels by manipulating amplitude responses F_{pq} approaching 1 or 0, defined as C_4^i routing of CP channels, as schematically illustrated by shining on or off bulbs in Fig. 4A in the main text.

It is worthwhile to note that in the current reported methods, elliptical polarization states are generally divided into two orthogonal circular polarizations with different ratios[S7-S9], which only concerns the weighted amplitude in CP components while ignores phase responses. However, in our work, we emphasize on the complex property of the decomposition coefficients of two CP components, which is originated from the non-zero inhomogeneity of such analogue-chiral Jones matrix and would provide extra freedoms for both amplitude and phase responses. Here we calculate and illustrate the plural coefficients $\boldsymbol{m}_{1,2}$ and $\boldsymbol{n}_{1,2}$ of two eigen-states of proposed meta-atoms. Figs. S22A – S22C present the amplitude profiles and Figs. S22D – S22F display the corresponding phase profiles of complex coefficients of the two eigen-states against the variable rotation angle θ_1, θ_2 and θ_3 of the three patches. We can observe that the amplitude and phase profiles of the decomposed coefficients $\boldsymbol{m}_{1,2}$ and $\boldsymbol{n}_{1,2}$ of eigen-state 1 vary severely while rotating the bottom patch of meta-atom, and the other eigen-state 2 maintains stable responses. Such results agree with the trajectories of two eigen-states on Poincaré sphere, which results from the axial asymmetric configuration of meta-atom with only variable θ_1. As for meta-atom with variable θ_2, the coefficients $\boldsymbol{m}_{1,2}$ and $\boldsymbol{n}_{1,2}$ are decomposed with amplitude and phase profiles, where the symmetric center of amplitude profiles of the two eigen-states are both 0.5 and that of phase profiles are 0 and π, respectively. When we rotate the top patch of meta-atom, the amplitude and phase profiles of $m_{1,2}$ and $n_{1,2}$ are just inversed to the situations of the rotated bottom patch, which is attributed to the reciprocity of the proposed multilayered configuration.

Based on the analyses on circular decomposition coefficients $\boldsymbol{m}_{1,2}$ and $\boldsymbol{n}_{1,2}$, the chiral gating and selecting responses, i.e. amplitudes of $\boldsymbol{F}_{uv}$, can be next verified. Here, we construct 13 typical analogue-chirality meta-atoms to achieve all scenarios of $\boldsymbol{C}_4^1$, $\boldsymbol{C}_4^2$, $\boldsymbol{C}_4^3$ and $\boldsymbol{C}_4^4$ gating results. The amplitude responses at the working frequency 10 GHz of all these meta-atoms are illustrated in Fig. S22G. The size of circle dots represents for the amplitude response, which illustrates that required gating and suppressed CP channels can be effectively realized. It is seen that the required CP gating effect can be successfully achieved by analogue-chirality meta-atoms, which provides the antecedent foundation for further metasurface constructions.

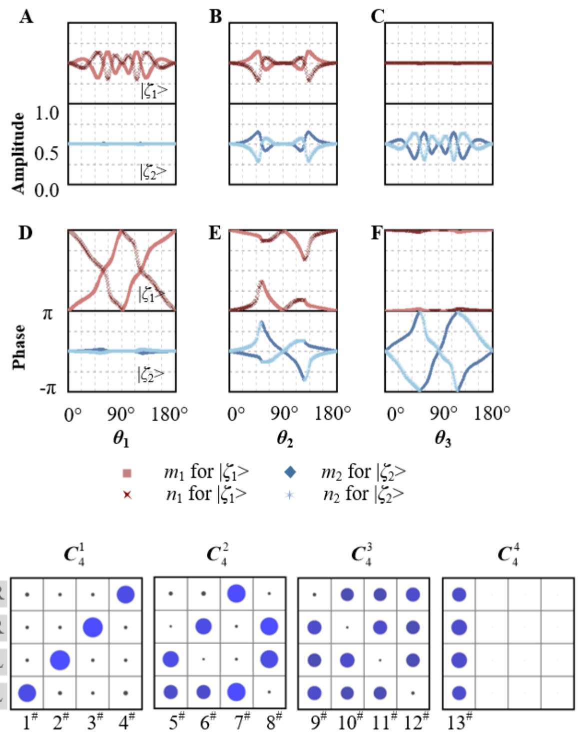

Fig. S22 Decomposed plural coefficients $m_{1,2}$ and $n_{1,2}$ of two eigen-states of meta-atom with variable (A) and (D) 1st layered patch with θ_1, (B) and (E) 2nd layered patch with θ_2, (C) and (F) 3rd layered patch with θ_3. (A), (B) and (C) present amplitude profiles and (D), (E) and (F) show phase profiles. (G) Amplitude responses of thirteen typical analogue-chirality meta-atoms to verify all scenarios of $\boldsymbol{C}_4^1$, $\boldsymbol{C}_4^2$, $\boldsymbol{C}_4^3$ and $\boldsymbol{C}_4^4$ gating results.

10.2 The calculated phase distributions of the target hologram image

In order to impose the required hologram images in the selected CP channels, we apply Gerchberg-Saxton (GS) imaging algorithm to calculate the spatial phase distributions of desired hologram images. The GS method is based on the reverse design according to the discretized target image as the virtual focusing points to calculate the total phase distributions on the pre-setting plane. Then, we utilize a metasurface platform to provide the point-to-point phase interruptions to achieve the calculated spatial phase distributions for the pre-defined hologram image on target plane. The phase interruptions Φ at specific coordination (x, y) on the metasurface plane can be described by:

$$\Phi(x,y)=\arg\left(\sum_{s=1}^{S}\frac{e^{ikr_t^s}}{r_t^s}\frac{\vec{\boldsymbol{E}}_s(x,y)}{\left|\vec{\boldsymbol{E}}_s(x,y)\right|}\right) \tag{S29}$$

where s donates the number of the focusing points of the discretized target image, t is the number of atom blocks on the metasurface plane, $\vec{\boldsymbol{E}}_s(x,y)$ shows the superimposed electric fields radiated from s focusing points, and r_t^s is the distance between t^{th} atom on metasurface plane and s^{th} focusing point.

In our work, we pre-set four distinct hologram characters "1", "2", "3", "4" and impose their phase profiles into the selected CP channels to illustrate the gating and suppressing effects. As for the image construction, we discretize character "1" into five focusing points (s = 5) with a wavelength interval, character "2" into eleven focusing points (s = 11), characters "3" and "4" into eleven and nine focusing points (s = 11 for "3" and s = 9 for "4"), respectively. The imaging plane is pre-set with a focusing length of $5\lambda_0$. As for the metasurface configuration, we design 31 × 31 meta-atoms along x- and y-axes. Thus, the total size of metasurface is $10.33\lambda_0 \times 10.33\lambda_0$, where the size of proposed non-orthogonal meta-atom is $0.33\lambda_0 \times 0.33\lambda_0$. Based on Eq. (S29), the calculated spatial phase distributions of character image are shown in Fig. S23, and the calculated ideal intensities of "1", "2", "3", "4" image are displayed in Fig. S24, where we can clearly observe the pre-defined characters with specific amount of focusing points.

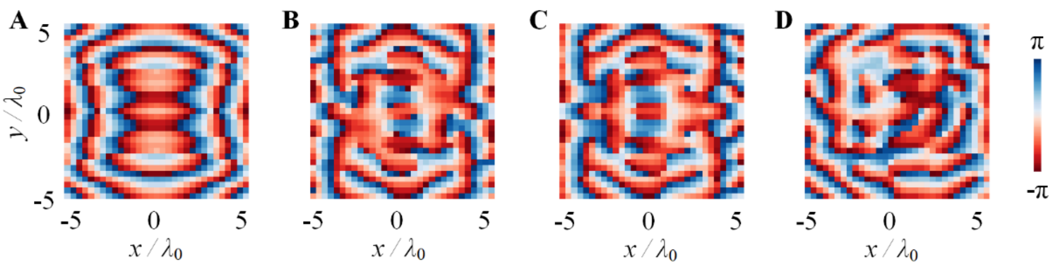

Fig. S23 Calculated spatial phase distributions of hologram image (A) "1", (B) "2", (C) "3", (D) "4".

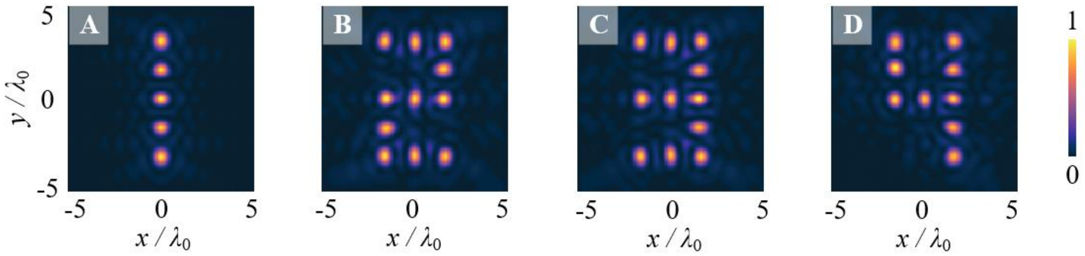

Fig. S24 Calculated energy intensity of hologram image (A) “1”, (B) “2”, (C) “3”, (D) “4”.

10.3 Synthetical phase modulation schemes for hologram manipulation in gated CP channels

As introduced in the main text, the artificial manipulation of unrestricted eigen-states can not only be applied in CP channel gating, but can also be utilized to impose required spatial phase distributions. We have verified that the distribution range of required CP gating conditions is independent of the phase responses of corresponding non-orthogonal meta-atom, which indicates that we can invoke extra DOFs to satisfy the required point-to-point phase interruptions. In this part, we introduce three distinct modalities to impose phase responses in different selected CP channels as follows (*S10*):

A. Chirality-assisted phase, is introduced by the relative rotation offset between distinct patch components that contributes to the normal-direction chirality configuration, which can effectively decouple the consistency between two co-polarized CP channels (L-L and R-R channels).

B. Propagation phase, tailored by constructive parameters along fast and slow axes of the in-plane shape of meta-atom, can impose independent phase responses between co- and cross-polarized channels (L-L and R-L channels or L-R and R-R channels).

C. Geometric phase, is modulated by the orientation angles of whole meta-atom constructions, which can impose conjugate phase profiles in two cross-polarized channels (R-L and L-R channels). Here we exhibit the utilized phase modalities for all $\boldsymbol{C}_4^i$ gating cases as shown in the following table S3.

Table S3. Utilized phase schemes to achieve distinct $\boldsymbol{C}_4^i$ gating with pre-defined images

	$\boldsymbol{C}_4^i$ **gating**	**Selected CP channels**	**Pre-defined images**	**Utilized phase modalities** **A**: Chirality-assisted phase **B**: Propagation phase **C**: Geometric phase
1#	$i = 1$	L-L	1	**A, B**

$2^{\#}$		R-L	2	**A, C**
$3^{\#}$		L-R	3	**A, C**
$4^{\#}$		R-R	4	**A, B**
$5^{\#}$	$i = 2$	L-L, R-L	1, 2	**A, B, C**
$6^{\#}$		L-L, L-R	1, 3	**A, B, C**
$7^{\#}$		L-L, R-R	1, 4	**A, B**
$8^{\#}$		R-L, L-R	2, 3	**B, C**
$9^{\#}$	$i = 3$	L-L, R-L, L-R	1, 2, 3	**A, B, C**
$10^{\#}$		L-L, R-L, R-R	1, 2, 4	**A, B, C**
$11^{\#}$		L-L, L-R, R-R	1, 3, 4	**A, B, C**
$12^{\#}$		R-L, L-R, R-R	2, 3, 4	**A, B, C**
$13^{\#}$	$i = 4$	L-L, R-L, L-R, R-R	1, 2, 3, 4	**A, B, C**

10.4 S parameters of the meta-atoms for non-orthogonal metasurface constructions

Here, we analyze the S parameters of the representative meta-atoms adopted for holographic metasurfaces constructions operating at 10 GHz frequency, as shown in Fig. S25. As for $\boldsymbol{C}_4^1$ gating on L-L channel, the amplitude and phase responses of 12 meta-atoms are displayed in Figs. S25A and S25B. High degree of contrast for the transmission coefficient between selected channel (L-L) and other three suppressed channels (R-L, L-R and R-R) are obviously observed, and the corresponding phase responses in L-L channel can cover the 2π-phase range. When two L-L and R-L channels are both selected for $\boldsymbol{C}_4^2$ gating, both amplitudes of $|\boldsymbol{F}_{LL}|$ and $|\boldsymbol{F}_{RL}|$ are obviously larger than that of $|\boldsymbol{F}_{LR}|$ or $|\boldsymbol{F}_{RR}|$, as shown in Fig. S25C. Meanwhile, phase responses $\angle\boldsymbol{F}_{LL}$ relies on propagation phase scheme that covers 2π for hologram generation, and $\angle\boldsymbol{F}_{RL}$ is the primary responses which can be further supplemented by geometric phase to perform the required phase distribution in R-L channel, as depicted in Fig. S25D. For $\boldsymbol{C}_4^3$ gating effect, we adopted 16 meta-atoms for construction and corresponding responses are displayed in Fig. S25E, where the average amplitudes in quadruplex channels are 0.63, 0.44, 0.44, 0.31, respectively. Notably, the contrast in the projected intensities when selecting three channels and suppressing one is not as distinct and uniform as for the previous two cases, due to the increased phase requirements for producing three independent holograms. Herein, $\angle\boldsymbol{F}_{LL}$ profile can still support 2π coverage, while the primary cross-polarized phase responses in R-L and L-R channels are also cover 2π, which would be decoupled by geometric phase for independent holograms, as shown in Fig. S25F. Meanwhile, Figs. S25G and Fig. S25H represent amplitude and phase responses of S parameters of non-orthogonal metasurface for full quadruplex holograms, whose average amplitudes are 0.57, 0.50, 0.50, 0.52, respectively, and four phase profiles can independently cover 2π by adopting chirality-assisted phase, propagation phase, and geometric phase, as illustrated in Note 10.3.

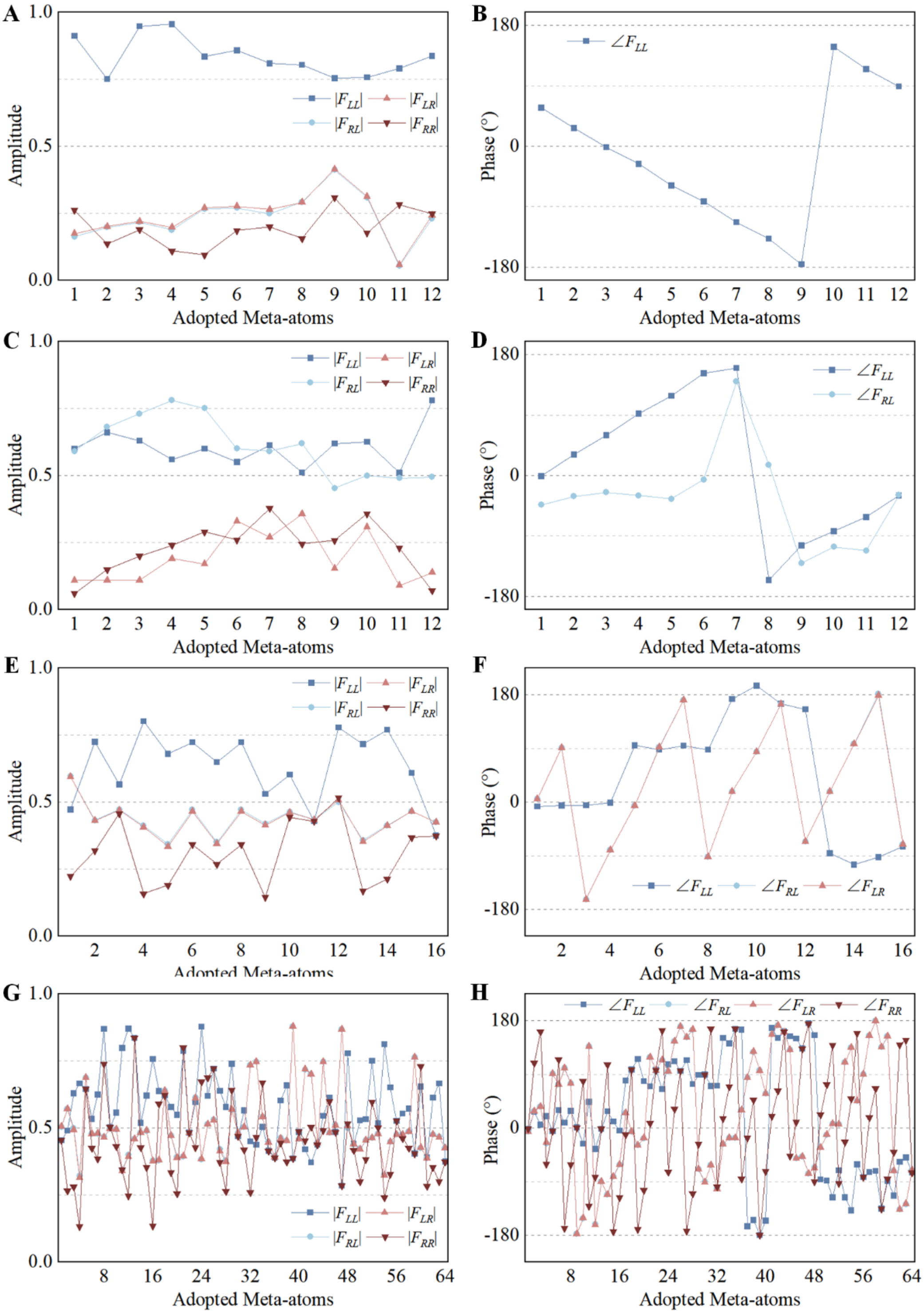

Fig. S25 Simulated S parameters at operation frequency 10 GHz of adopted meta-atoms for non-orthogonal metasurface constructions with (A) amplitude and (B) phase responses with $\boldsymbol{C}_4^1$ for L-L channel, (C) amplitude and (D) phase responses with $\boldsymbol{C}_4^2$ for L-L and R-L channels, (E) amplitude and (F) phase responses with $\boldsymbol{C}_4^3$ for L-L, R-L and L-R channels, (G) amplitude and (H) phase responses with $\boldsymbol{C}_4^4$ for full channels, respectively.

10.5 Supplementary simulation and measurement results for $\boldsymbol{C}_4^i$ gating of CP channels

In main text, we have illustrated the theoretical mechanism and experimental verification of $\boldsymbol{C}_4^i$ gating of CP channels and impose desired hologram image in the selected transmitting channels. We exhibit the demonstrations of $\boldsymbol{C}_4^1$ gating only with imposed hologram image "1" in L-L channel, $\boldsymbol{C}_4^2$ gating with "1" in L-L channel and "2" in R-L channel, $\boldsymbol{C}_4^3$ gating with "1" , "2" , "3" in L-L, R-L and L-R channels, $\boldsymbol{C}_4^4$ gating with images "1" , "2" , "3" , "4" in all four channels. Here we supplement energy distributions and efficiencies of other $\boldsymbol{C}_4^i$ gating scenarios.

First, as for the $\boldsymbol{C}_4^1$ (i = 1) gating functionalities, we construct four separate samples in total to select separate L-L, R-L, L-R or R-R channels and simultaneously suppress the other three channels, while imposing distinct hologram image "1", "2", "3", "4" into each selected channel. Fig. S26 presents the simulated and measured results of four proposed samples for all $\boldsymbol{C}_4^1$ gating functions. We can clearly observe that the gated CP channel is lightened with the pre-set image, where L-L channel is selected and imposed with character "1", R-L channel is gated with character "2", L-R channel is selected with character "3" and R-R channel is imposed with character "4", while other three channels are suppressed. The agreement between simulated and measured results indicates the feasibility of the proposed CP channel gating mechanism. For the $\boldsymbol{C}_4^2$ (i = 2) gating effect, we propose three samples to gate arbitrary two CP channels, including L-L and R-L, L-L and L-R, L-L and R-R selection examples. It is necessary to explain that we abandon to fabricate R-L and L-R selection since that such CP gating function is equal to those works on cross-polarized decoupling effect of orthogonal circular polarizations, which has been widely studied from microwave to optical regimes[S11-S15]. Here the aim of our work is to exhibit the general mechanism for arbitrary CP channel gating and controlling. Thus, we only demonstrate the unexplored gating functions in this part. Fig. S27 shows the simulated and measured energy intensity of the metasurface samples to select L-L and R-L with imposed image “1” and “2”, L-L and L-R with “1” and “3”, and L-L and R-R with “1” and “4”, respectively. We can see that the energy distributions of unselected CP channels of corresponding metasurfaces approach zero as anticipated. Next, we demonstrate the functionality of $\boldsymbol{C}_4^3$ ($i = 3$) gating through two metasurface samples, one is designed to select L-L, R-L and L-R with imposed “1”, “2”, “3”, respectively, and the other is proposed to achieve gated L-L, R-L and R-R with imposed “1”, “2”, “4”. As known, the $\boldsymbol{C}_4^3$ function of L-L, R-L and L-R with “1”, “2”, “3” is reciprocal to that of R-L, L-R and R-R with “2”, “3”, “4”, while L-L, R-L and R-R with “1”, “2”, “4” is reciprocal to that of L-L, L-R and R-R with “1”, “3”, “4”. Thus, we only fabricate two typical examples to verify the $\boldsymbol{C}_4^3$ effect, and the corresponding simulated and measured results are shown in Fig. S28. As mentioned before, there totally exists four CP channels and the $\boldsymbol{C}_4^4$ ($i = 4$) gating function only require one specific demonstration, where the four channels are lighted by image “1”, “2”, “3”, “4”, respectively. The simulated and measured energy intensities are exhibited in Fig. S29 and also in Fig. 4C in the main text. It has to be noticed that for the case of $\boldsymbol{C}_4^2$, $\boldsymbol{C}_4^3$ and $\boldsymbol{C}_4^4$, we use the same colorbar for all the hologram images in the measurement of each separate metasurface. Since there are less pixel points for the image “1”, its hologram image is more brilliant than the other ones.

Additionally, the measured transmission efficiency of all these ten fabricated metasurface samples are illustrated in Fig. S30. The transmitted efficiency gap between the selected and suppressed CP channels convincingly proves the CP gating effect of the proposed metasurface samples.

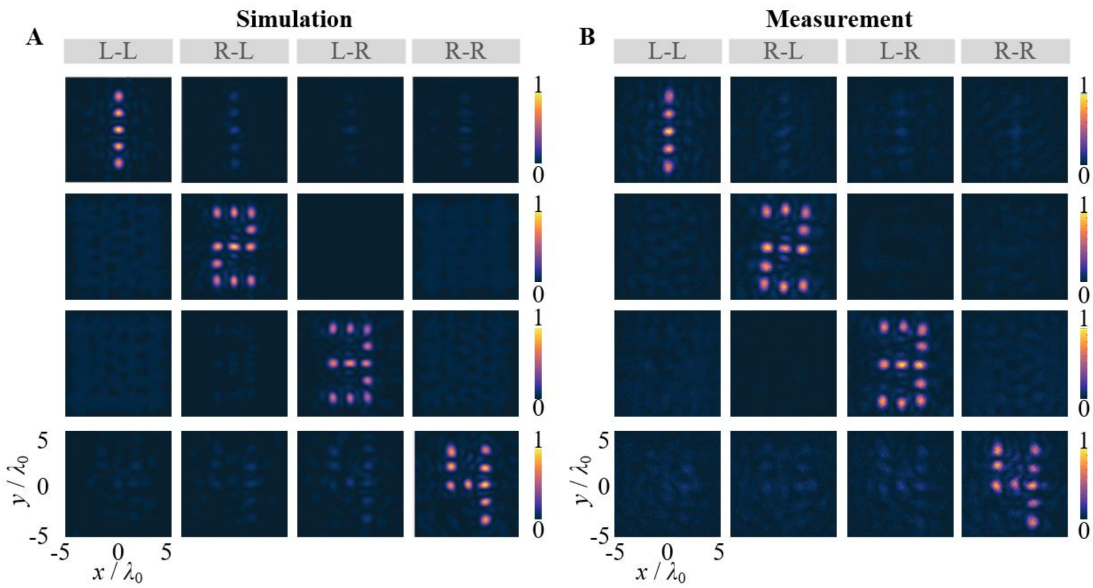

Fig. S26 Demonstration of C_4^1 gating for L-L, R-L, L-R, R-R channel, separately. (A) Simulated and (B) measured hologram images in *xoy* plane with distance z = $5\lambda_0$ in all CP transmitting channels.

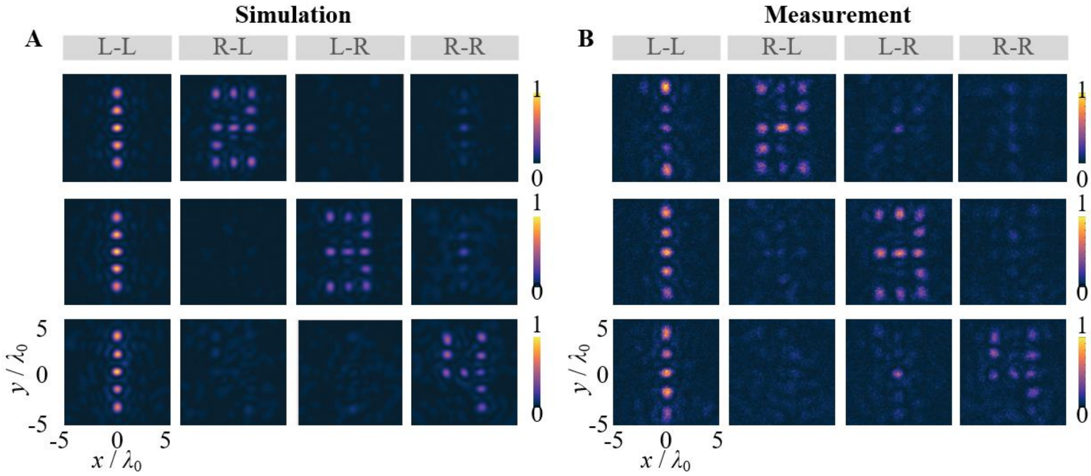

Fig. S27 Demonstration of C_4^2 gating for L-L and R-L, L-L and L-R, L-L and R-R channels, respectively. (A) Simulated and (B) measured hologram images in *xoy* plane with distance z = $5\lambda_0$ in all CP transmitting channels.

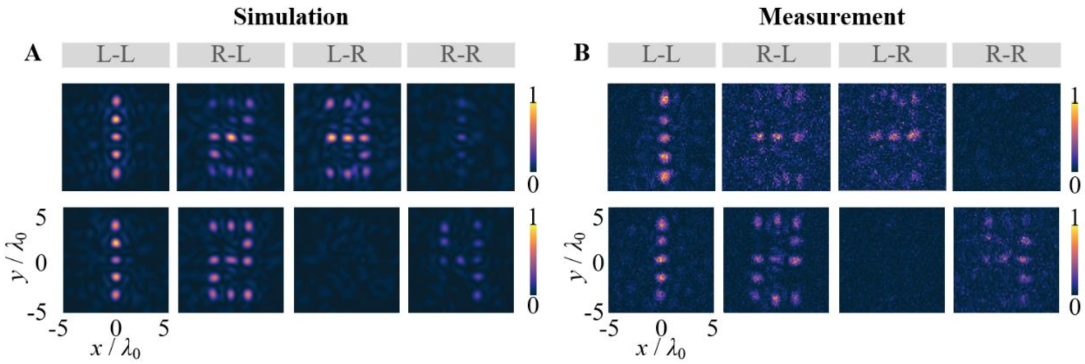

Fig. S28 Demonstration of C_4^3 gating for L-L, R-L and L-R, L-L, R-L and R-R channels, respectively. (A) Simulated and (B) measured hologram images in *xoy* plane with distance z = $5\lambda_0$ in all CP transmitting channels.

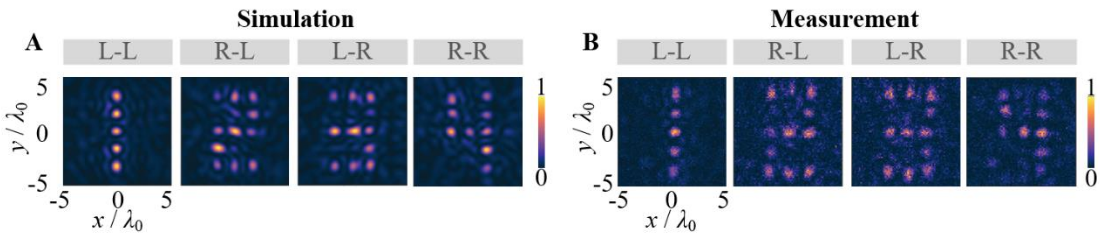

Fig. S29 Demonstration of C_4^4 gating for all four channels. (A) Simulated and (B) measured hologram images in *xoy* plane with distance z = $5\lambda_0$ in all CP transmitting channels

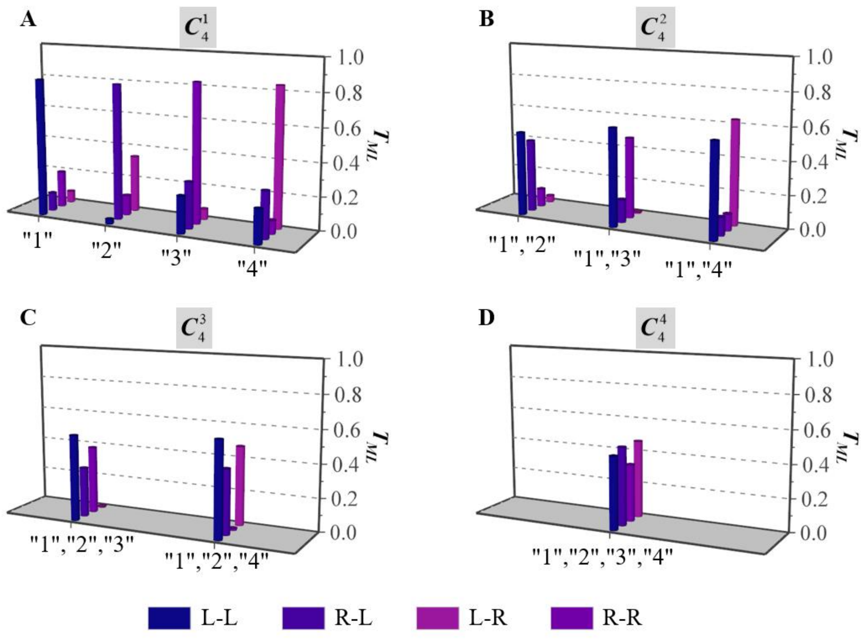

Fig. S30 Measured transmission efficiencies of all fabricated samples. (A) Four meta-lenses for C_4^1 gating. (B) Three meta-lenses for C_4^2 gating. (C) Two meta-lenses for C_4^3 gating. (D) Meta-lens for C_4^4 gating.

10.6 Analyzing the holographic intensity distribution

Considering the one channel scenario, as illustrated in Fig. 4C, we observed crisp holographic projection. Increasing the number of channels as for consequence to degrade the imaging qualities of the holograms due to the polarization multiplexing.

(ii) *In design*, the limitations associated to the holographic projection quality are primarily related to the non-ideal phase responses of the meta-atoms. In our work, each non-orthogonal metasurface sample is composed of 31 × 31 meta-atoms, which should satisfy the required discretized phase distributions for all multiplexed polarization channels, while simultaneously comply with the required channel gating effects. Increasing the number of polarization conversion channels thus imposes additional phase profiles that would simultaneously match the phase profile requirement of each CP channel independently. As the phase distribution varies from pixel to pixel and from channel to channels at each pixel, we have to find a compromise within the available phase resources, each pixel at the time.

(iii) *In experiment*, the near-field mapping experiment is conducted in an anechoic chamber, but unavoidable disturbances, including spurious diffractions from the chamber, would create undesired interferences and thus add additional noise on the images. The transmitting source is made from a horn antenna. It can launch LHCP or RHCP plane waves, in agreement with the simulated conditions. The propagation distance between the transmitting antenna and the sample is chosen to exceed $20\lambda_0$, so as to achieve quasi-plane wave input wave profile. Some residual spherical curvature on the incident wave-front cannot be totally eliminated, producing phase discrepancy between the center and the edges of metasurfaces, which would further exhibit natural expansion and affect the output hologram profile. Due to the finite surrounding absorbing materials around the fabricated sample, as shown in Fig. S14B, complex spurious interferences between the hologram and the reflected fields occur at the imaging plane. Since the receiver probe is driven by a motion controller, which introduce minute mechanical vibration during measurement, disturbing the collected electric field information and introducing inevitable noises in the hologram intensity profiles.

To conclude, the quality of measured holograms is limited due to the mechanism used for the projection, the hologram designs themselves, and the uncertainties in the experimental setup. Imaging resolution can be enhanced by exploiting neural-network based amplitude-phase imaging algorithm and optimizing measurement schemes. Although there exist some imperfections in the proof-of-concept demonstration of multiplexed holograms, the feasibility of the proposed non-orthogonal eigen formalism and its potentials in reaching the efficiency limit have been validated.

10.7 Bandwidth performances of C_4^i gating of CP channels

Here, we supplement the bandwidth performances of the CP selective and hologram demonstrations. The measured holographic distributions of all four representative samples at 9.50 GHz, 9.75 GHz, 10.00 GHz, 10.25 GHz, and 10.50 GHz are exhibited in Fig. S31. As illustrated in the main text, these four metasurfaces are constructed to obtain $\boldsymbol{C}_4^1$ gating with hologram image "1" in L-L channel, $\boldsymbol{C}_4^2$ gating with "1" in L-L channel and "2" in R-L channel, $\boldsymbol{C}_4^3$ gating with "1" , "2" , "3" in L-L, R-L and L-R channel, $\boldsymbol{C}_4^4$ gating with "1" , "2" , "3" , "4" in all four channels, respectively. Required distinct holographic image is effectively imposed in the selected channels as desired within the bandwidth. There exist some distortions in hologram characters when deviating from center frequency, attributing to the fact that corresponding spatial phase distribution functions are all calculated at the center frequency 10 GHz to simultaneously guarantee the optimal CP selectivity effect. With the shift of working frequency, the corresponding phase responses are accordingly dispersed, resulting in the slight deviations and errors in the holistic wavefronts. In future work, we will try to explore achromatic stacking twisted metasurface to suppress the dispersion.

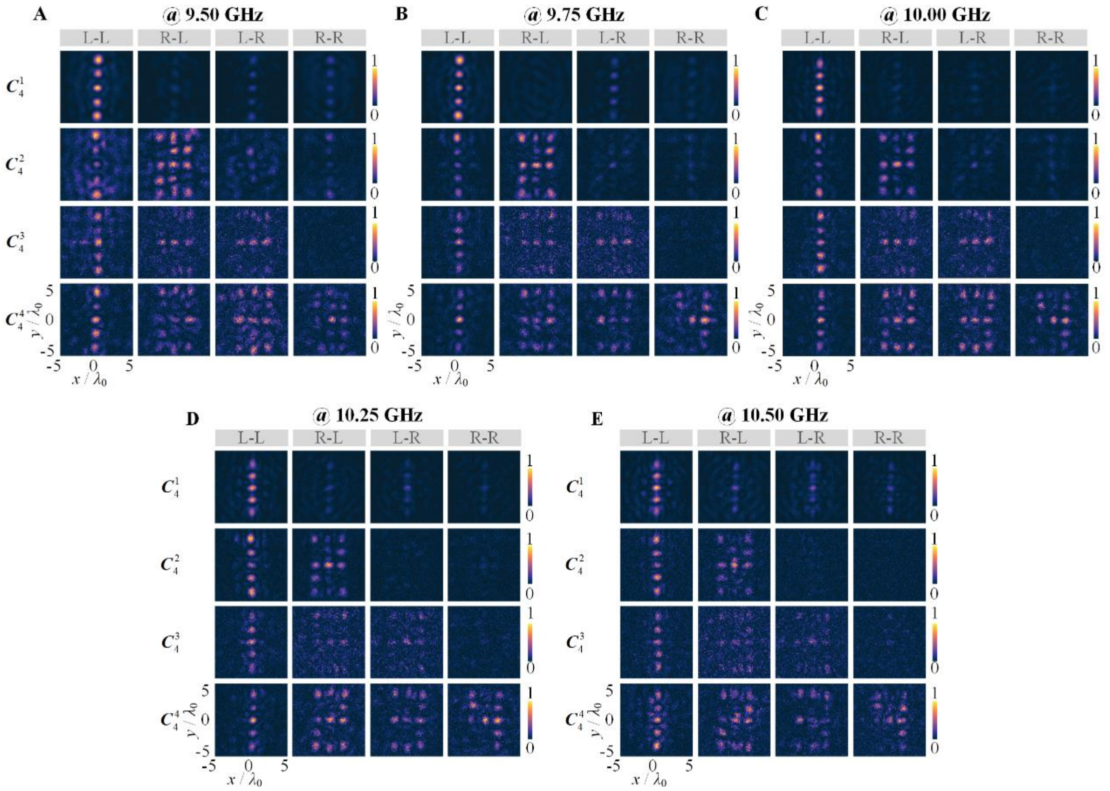

Fig. S31 Measured energy distributions in detection planes of four representative samples for achieving $\boldsymbol{C}_4^1$, $\boldsymbol{C}_4^2$, $\boldsymbol{C}_4^3$ and $\boldsymbol{C}_4^4$ gating effects at (A) 9.50 GHz, (B) 9.75 GHz, (C) 10.00 GHz, (D) 10.25 GHz, (E) 10.50 GHz, respectively.

10.8 Merit of imaging and cross-talk analyses of holographic imaging

It is essential to quantitatively analyze the imaging quality of all produced holographic characters. Here, we adopt correlation coefficient $\boldsymbol{\rho_0}$ between measured hologram pattern and the corresponding calculated imaging (Fig. S24) to characterize the imaging quality, as calculated by:

$$\boldsymbol{\rho_0}\left(\boldsymbol{I}_{cal},\boldsymbol{I}_{mea}\right)=\frac{COV\left(\boldsymbol{I}_{cal},\boldsymbol{I}_{mea}\right)}{\sqrt{D\left(\boldsymbol{I}_{cal}\right)}\sqrt{D\left(\boldsymbol{I}_{mea}\right)}} \tag{S30}$$

where $COV\,(\boldsymbol{I}_{cal}, \boldsymbol{I}_{mea})$ is the covariance of theoretically calculated hologram intensity $\boldsymbol{I}_{cal}$ and measured energy intensity $\boldsymbol{I}_{mea}$, and $D(\boldsymbol{I}_{cal})$ and $D(\boldsymbol{I}_{mea})$ shows the variances of corresponding intensities, respectively. The measured correlation coefficient ρ_0 of these four samples within the bandwidth 9 GHz – 11 GHz are illustrated in Fig. 4E in main text. The contrast ratio of ρ_0 profiles in the selected and unselected channels can obviously verify CP routing effect of the proposed scheme. Around center operating frequency of 10 GHz, correlation coefficients of the measured holographic imaging reach 75% when the single channel is selected. It is seen that the quality coefficient ρ_0 of imposed imaging are deteriorated with the increase of gated channels or complicate reconstructed patterns. This is primarily due to the adopted reconstruction holographic algorithm relying on virtual discrete phase sources. The discontinuous phase distributions contribute to the unpredictable interferences around focusing points in target holographic pattern, which would inherently affect the imaging quality. Besides, with more CP channels routed, more phase freedoms need to be balanced and supplemented, and the resolution of reconstructed patterns in different channels would accordingly be compensated and restricted from each other. This imaging resolution limit can be further optimized by neural network based amplitude-phase holographic algorithms in future research.

Furthermore, we analyze the cross-talk between different CP channels by adopting correlation coefficient $\boldsymbol{\rho}_{mn}$:

$$\boldsymbol{\rho}_{mn}\left(\boldsymbol{I}_m,\boldsymbol{I}_n\right)=\frac{COV\left(\boldsymbol{I}_m,\boldsymbol{I}_n\right)}{\sqrt{D\left(\boldsymbol{I}_m\right)}\sqrt{D\left(\boldsymbol{I}_n\right)}} \tag{S31}$$

where m and n denote the selected specific one of L-L, R-L, L-R, R-R channels, COV ($\boldsymbol{I}_m$, $\boldsymbol{I}_n$) is the covariance of measured hologram intensities $\boldsymbol{I}_m$ and $\boldsymbol{I}_n$ in different m^{th} and n^{th} channels, and $D(\boldsymbol{I}_m)$ and $D(\boldsymbol{I}_n)$ shows the variances of corresponding intensities, respectively. It is worth to clarify that in our design, all the target holographic characters are set in the middle of the imaging area, and the discrete points in "1", "2", "3", "4" are partly overlapped. If we adopt the whole output energy distributions in distinct CP channels to calculate correlation coefficient $\boldsymbol{\rho}_{mn}$, there must exist serious dependence which cannot properly express actual results. For example, when we calculate $\boldsymbol{\rho}_{mn}$ between "1" in L-L channel and "2" in L-R channel as shown in Fig. S32, the focusing points in 1st, 3rd, 5th circle regions of pattern "1" are completely overlapped with those in 2nd, 6th, 10th of pattern "2", and the energy distributed in these overlapped circle areas would disturb correlation performance. Thus, before the correlation coefficient $\boldsymbol{\rho}_{mn}$ calculation, we block "the effective signals" in the measured hologram intensities to be processed. Likewise in Fig. S32, if we want to characterize the cross-talks that produced by "1" in L-L on "2" in R-L channel, the energy distributions in the 11 circle regions (labelled as "the effective signals") in imaging "2" are blocked firstly. Then we adopt Eq. S31 to calculate $\boldsymbol{\rho}_{mn}$, where $\boldsymbol{I}_m$ is regarded as the target imaging while $\boldsymbol{I}_n$ actually presents a preprocessed imaging with blocked "the effective signals".

Based on above settings, measured $\boldsymbol{\rho}_{mn}$ of these four metasurface samples at 10 GHz are illustrated in Fig. 4F in main text. When $m = n$, the measured $\boldsymbol{\rho}_{mn}$ equals to 1 as presented in the diagonal line, and when $m \neq n$, $\boldsymbol{\rho}_{mn}$ denotes cross-talks between distinct channels. Noting that metasurface with $\boldsymbol{C}_4^1$ gating of L-L channel, the cross-talks produced by imaging "1" in R-L, L-R and R-R channels are 6%, 38.5% and 36.6%, respectively. The high cross-talks in R-L and R-R channels are due to the phase errors from discretization and amplitude sacrifices of meta-atoms, which can be further suppressed through configuration optimizations to provide eigen-formalism with high matching degree. Meanwhile, the other cross-talks in multiple channel selections are all lower than 10%, indicating the feasibility of the proposed scheme.

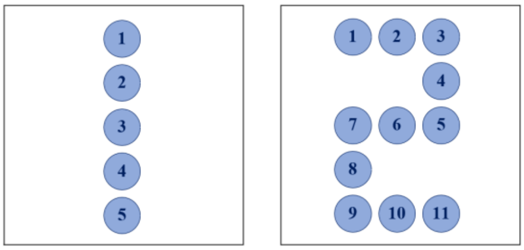

Fig. S32 Approach illustration for crosstalk calculation.

References

S1. S. Y. Lu, R. A. Chipman, Homogeneous and inhomogeneous Jones matrices. *Journal of the Optical Society of America A* **11**, 766-773 (1994).

S2. T. Tiberiu, Generalized observables in polarization optics. *Journal of Physics A: Mathematical and General* **36**, 9577 (2003).

S3. Y. Zhao, M. A. Belkin, A. Alù, Twisted optical metamaterials for planarized ultrathin broadband circular polarizers. *Nature Communications* **3**, 870 (2012).

S4. Y. Zhao *et al.*, Chirality detection of enantiomers using twisted optical metamaterials. *Nature Communications* **8**, 14180 (2017).

S5. N. Liu, H. Liu, S. Zhu, H. Giessen, Stereometamaterials. *Nature Photonics* **3**, 157-162 (2009).

S6. M. Decker *et al.*, Strong optical activity from twisted-cross photonic metamaterials. *Optics Letters* **34**, 2501-2503 (2009).

S7. H. Yang *et al.*, All-dielectric metasurface for fully resolving arbitrary beams on a higher-order Poincaré sphere. *Photonics Research* **9**, 331-343 (2021).

S8. Q. Song *et al.*, Ptychography retrieval of fully polarized holograms from geometric-phase metasurfaces. *Nature Communications* **11**, 2651 (2020).

S9. Q. Song *et al.*, Bandwidth-unlimited polarization-maintaining metasurfaces. *Science Advances* **7**, eabe1112 (2021).

S10. Y. Yuan *et al.*, Independent phase modulation for quadruplex polarization channels enabled by chirality-assisted geometric-phase metasurfaces. *Nature Communications* **11**, 4186 (2020).

S11. J. P. B. Mueller, N. A. Rubin, R. C. Devlin, B. Groever, F. Capasso, Metasurface polarization optics: independent phase control of arbitrary orthogonal states of polarization. *Physical Review Letters* **118**, 113901 (2017).

S12. G. Ding *et al.*, Dual-helicity decoupled coding metasurface for independent spin-to-orbital angular momentum conversion. *Physical Review Applied* **11**, 044043 (2019).

S13. M. Liu *et al.*, Broadband generation of perfect Poincaré beams via dielectric spin-multiplexed metasurface. *Nature Communications* **12**, 2230 (2021).

S14. Y. Guo *et al.*, Spin-decoupled metasurface for simultaneous detection of spin and orbital angular momenta via momentum transformation. *Light: Science & Applications* **10**, 63 (2021).

S15. Y. Qiu, S. Tang, T. Cai, H. Xu, F. Ding, Fundamentals and applications of spin-decoupled Pancharatnam—Berry metasurfaces. *Frontiers of Optoelectronics* **14**, 134-147 (2021).